

# Lattice Boltzmann study of mass transfer for two-dimensional Bretherton/Taylor bubble train flow

A. Kuzmin<sup>\*,a</sup>, M. Januszewski<sup>b</sup>, D. Eskin<sup>c</sup>, F. Mostowfi<sup>c</sup>, J.J. Derksen<sup>a</sup>

<sup>a</sup>*Chemical and Materials Engineering, University of Alberta  
7th Floor, ECERF, 9107 116 St, Edmonton, Alberta, T6G 2V4 Canada*

<sup>b</sup>*Institute of Physics, University of Silesia, 40-007 Katowice, Poland*

<sup>c</sup>*Schlumberger DBR Technology Center  
9450 17 Ave NW, Edmonton, Alberta, T6N 1M9 Canada*

---

## Abstract

This work presents a procedure for the determination of the volumetric mass transfer coefficient in the context of lattice Boltzmann simulations for the Bretherton/Taylor bubble train flow for capillary numbers  $0.1 < Ca < 1.0$ . We address the case where the hydrodynamic pattern changes from having a vortex in a slug ( $Ca < 0.7$ ) to not having it ( $Ca > 0.7$ ) [1]. In the latter case the bubble shape is asymmetric and cannot be approximated through flat surfaces and circular circumferences as is often done in the literature [2, 3]. When the vortex is present in the slug, the scalar concentration is well mixed and it is common to use periodic boundary conditions and the inlet/outlet-averaged concentration as the characteristic concentration. The latter is not valid for flows where the tracer is not well mixed, i.e.  $Ca > 0.7$ . We therefore examine various boundary conditions (periodic, open, open with more than 1 unit cell) and definitions of the characteristic concentration to estimate mass transfer coefficients for the range of capillary numbers  $0.1 < Ca < 1.0$ . We show that the time-dependent volume averaged concentration taken as the characteristic concentration produces the most robust results and that all strategies presented in the literature are extreme limits of one unified equation. Finally, we show good agreement of simulation results for different Peclet numbers with analytical predictions of van Baten and Krishna [2].

---

\*Corresponding author

*Email addresses:* kuzmin@ualberta.ca (A. Kuzmin), michal.j@gmail.com (M. Januszewski), deskin@slb.com (D. Eskin), fmostowfi@slb.com (F. Mostowfi), jos@ualberta.ca (J.J. Derksen)

*Key words:* Mass Transfer, Taylor/Bretherton bubble train flow, Multiphase flow, Lattice Boltzmann method, Binary liquid model, Flow in microchannels with parallel plates

---

## 1. Introduction

Monolith reactors have recently been getting more attention as a promising alternative to slurry reactors and trickle bed reactors [3, 4]. These reactors usually operate in the Bretherton-Taylor regime [5, 6] which is a flow of equally sized, long air bubbles through a liquid medium, see Fig. 1. This flow regime is characterized by the dominance of surface tension over inertia and viscous effects, and by comparatively small gas flow velocities [7]. Due to the dominance of surface tension, the flow exhibits advantageous properties which cannot be achieved in its macroscopic counterparts: liquid thin films [5] between bubbles and walls strongly enhance mass transfer from gas and walls to liquid; the plug flow regime occurring in monolith reactors allows to perform chemical reactions in slugs only [3]. Moreover, the low slip velocity between gas and liquid is utilized in experiments to measure liquid velocity [6]: bubbles travelling with approximately the same velocity as liquid can be captured with a camera. These properties explain why nowadays one can find a large number of applications of the Bretherton-Taylor bubble train flow: continuous flow analyzers to measure liquid velocity, chemical reactors for hydrogenation of nitroaromatics, 2-ethyl-hexenal, Fischer-Tropsch synthesis, etc. The extensive reviews of Kreutzer et al. [3], Gupta et al. [8], Yue et al. [7] cover a significant number of applications.

This work is focused on gas to liquid mass transfer for the two-dimensional Bretherton/Taylor flow. A good understanding of mass transfer and how it depends on parameters such as the capillary number, the Reynolds number, and slug and bubble lengths allows to properly manufacture a microchannel with properties necessary to ensure that chemical reactions are performed in the best possible manner. The mass transfer coefficient is defined as the flux from the gas-liquid interface divided by the difference of the imposed concentration and the characteristic concentration in the domain. The concentration distribution in the domain is prescribed by underlying hydrodynamics fields. For example, experimental studies [7, 4] show a complex dependency of the mass transfer coefficient on flow parameters: bubble and slug lengths, and bubble velocity, which in turn relate to the capillary number  $Ca$  and the

Reynolds number  $Re$ . Yue et al. [7] established an experimental correlation for the volumetric mass transfer coefficient for a bubble train as a function of the diffusion coefficient, slug and bubble lengths, and bubble velocity:

$$k_L a = \frac{2}{d_h} \left( \frac{DU_{\text{bubble}}}{L_{\text{bubble}} + L_{\text{slug}}} \right)^{0.5} \left( \frac{L_{\text{bubble}}}{L_{\text{bubble}} + L_{\text{slug}}} \right)^{0.3}, \quad (1)$$

where  $k_L a$  is the volumetric mass transfer coefficient,  $d_h$  is the hydraulic diameter,  $L_{\text{bubble}}$  is the bubble length,  $L_{\text{slug}}$  is the slug distance (between bubbles),  $U_{\text{bubble}}$  is the bubble velocity, and  $D$  is the diffusion coefficient.

The understanding of mass transfer for the bubble train flow is not possible without knowledge of hydrodynamic patterns. There are several works studying the hydrodynamic properties of the bubble train flow, both experimental [9, 10, 11] and numerical [12, 13, 1, 14]. For the flow of long bubbles between parallel plates chosen here as the study case, it is indicated that there exists a vortex in the liquid slug for  $Ca < 0.7$ , see Fig. 7, and that the bubble shape is symmetric for low capillary numbers ( $Ca < 0.1$  [11]) with the capillary number defined as:

$$Ca = \frac{\mu_{\text{liq}} U_{\text{bubble}}}{\gamma}, \quad (2)$$

where  $\mu_{\text{liq}}$  is the liquid viscosity,  $U_{\text{bubble}}$  is the bubble velocity, and  $\gamma$  is the interfacial tension. The fact that the bubble shape for  $Ca < 0.1$  can be represented as two hemicircles and two planar interfaces with the vortex existing in the liquid slug has been utilized for analytical estimations of mass transfer properties.

Since the mass transfer coefficient is defined in terms of a mass flux through a certain area, Eq. 5, analytical estimates [3, 15] are based on a decomposition of the bubble surface in parts. The mass transfer coefficient is calculated through two separate contributions from two planar films and two hemicircles. For both contributions the Higbie penetration theory [16] is utilized, which states that the mass transfer coefficient for a simple flow geometry depends on the average time a liquid packet interacts with a geometrical feature. It can be calculated as  $\sqrt{\frac{\pi D}{t_{\text{char}}}}$ , where  $t_{\text{char}}$  is the interaction time. As an example of the application of the Higbie penetration theory, the mass transfer coefficient for the flow of bubbles between parallel plates is calculated as (similar to the work of van Baten and Krishna [2]):

$$k_L = 2\sqrt{\frac{\pi D}{t_{\text{film}}}} + 2\sqrt{\frac{\pi D}{t_{\text{circle}}}}, \quad (3)$$

29 where  $t_{\text{film}} = \frac{L_{\text{film}}}{U_{\text{bubble}}}$  stands for the interaction time of liquid traveling next to  
 30 the planar part of the bubble, and  $t_{\text{circle}} = \frac{\pi R_{\text{circle}}}{U_{\text{bubble}}}$  is the time during which the  
 31 liquid in the slug travels the distance of half the bubble cap circumference.

32 Despite their simplicity, such analytical expressions work well for flows  
 33 with low capillary numbers  $Ca < 0.1$  [4] where the bubble shape is symmet-  
 34 rical and can be approximated with good precision. Moreover, because of  
 35 the hydrodynamic pattern in the slug (i.e. presence of a vortex in slug), one  
 36 can estimate the time for a fluid batch to travel the whole circumference.  
 37 However, with the increase of the capillary number the situation changes  
 38 significantly – the symmetrical bubble shape is lost and the bubble resem-  
 39 bles a bullet [17]. For flows with  $Ca > 0.7$  there is also no vortex in the  
 40 liquid slug. In this case the Higbie theory fails to estimate the contribution  
 41 from bubble caps, which explains the need to turn to numerical simulations  
 42 where all hydrodynamic fields as well as complex bubble shapes are taken  
 43 into account.

44 Typical numerical studies of mass transfer [3, 2] do not consider the sim-  
 45 ulation of bubble shapes for  $Ca > 0.1$ . The usual simulation of mass transfer  
 46 is performed as follows:

47 **I** The bubble shape is calculated either through analytical correlations [5] or  
 48 experimental correlations [11] without directly resolving bubble shapes  
 49 through multiphase simulations. The expressions for bubble shapes are  
 50 available only for flows with capillary number  $Ca < 0.1$ .

51 **II** Hydrodynamic fields are then obtained by performing simulations of one-  
 52 component flow around the bubble by imposing the bubble velocity on  
 53 the channel walls. Thus, the simulations are performed in the reference  
 54 frame moving with the bubble. A stress-free condition is imposed at  
 55 the bubble surface.

**III** The mass transfer simulations are performed in the reference frame mov-  
 ing with the bubble. The saturation concentration is imposed at the  
 bubble surface. Only one unit cell containing a single bubble is used for  
 simulations. Periodic concentration boundary conditions are utilized to  
 determine the volumetric mass transfer coefficient, which is calculated  
 through the following equation [2]:

$$k_L a = \frac{\overline{\text{Flux}}}{C_{\text{bubble}} - \langle C_{\text{in/outlet}} \rangle} \frac{\text{bubble surface area}}{\text{unit cell volume}}, \quad (4)$$

56 where  $\langle C_{\text{in/outlet}}(t) \rangle = \int C U_{\text{in/outlet}} dA / \int U_{\text{in/outlet}} dA$  is the space-averaged  
 57 inlet/outlet (periodic boundary conditions) concentration as a function  
 58 of time. Therefore, in terms of the mass transfer definition,  $\langle C_{\text{in/outlet}}(t) \rangle$   
 59 plays the role of the characteristic concentration. The time-averaged  
 60 concentration flux ( $\overline{\text{Flux}}$ ) is calculated as the difference between the  
 61 overall average concentration in the whole domain ( $\langle C_{\text{overall}} \rangle = \int_V C dV / V$ )  
 62 at time  $t_1$  and at time  $t_2$  divided by the time difference  $t_2 - t_1$ . The  
 63 agreement between numerical simulations [2] and experimental corre-  
 64 lations of Bercic and Pintar [4] was good.

65 The presented numerical approaches [2, 3] can be criticized on a number of  
 66 points. They mainly relate to the bubble shape approximation, which is taken  
 67 to be symmetrical, i.e. consisting of two hemispheres and film for the case  
 68 of flow in circular capillaries. This is valid for small capillary numbers only  
 69 ( $Ca < 0.1$ ). As previously discussed, for such capillary numbers the tracer  
 70 is well mixed in the slug and the choice of the characteristic concentration  
 71 needed for the mass transfer coefficient, Eq. 5, is obvious. With minimal  
 72 differences in the results, it can either be the averaged concentration in the  
 73 liquid slug or the inlet/outlet space-averaged concentration. The latter is  
 74 used in the formulation of van Baten and Krishna [2] presented above.

75 While it is clear that periodic boundary conditions can be employed for  
 76 the calculation of hydrodynamic fields, the same does not apply to the mass  
 77 transfer coefficient simulations. Experimental correlations [4] show that the  
 78 concentration in a bubble train along the streamwise direction changes ex-  
 79 ponentially with distance. Mass transfer simulations however, are made only  
 80 for one unit cell using periodic boundary conditions with the same concen-  
 81 tration at the inlet and at the outlet. The question is how single unit cell  
 82 simulation corresponds to experimental measurements arises where concen-  
 83 tration difference is measured at the distances of at least a few unit cells [4].  
 84 In other words, one needs to understand how the discrete one unit cell simu-  
 85 lation corresponds to the continuous picture in experiments where one does  
 86 not distinguish discrete bubbles but takes measurements of concentration at  
 87 different locations.

88 Addressing situations for a rich number of hydrodynamic patterns, shapes,  
 89 and effects of bubble lengths, etc for bubble train flows, we feel that there is  
 90 a need to examine carefully the strategies and assumptions behind the nu-  
 91 merical calculations of the mass transfer coefficient. We aim at establishing  
 92 clear procedures as to how properly obtain the mass transfer coefficient via a

93 study of different boundary conditions and different definitions of the char-  
 94 acteristic concentration. The case we want to examine is a two-dimensional  
 95 bubble train flow between parallel plates. We address the following issues:

96 **I** Applicability of periodic boundary conditions to determine the mass trans-  
 97 fer coefficient when the vortex in the slug disappears, i.e. when  $Ca >$   
 98 0.7.

99 **II** Validity of the inlet/outlet-averaged or domain-averaged concentrations  
 100 as characteristic concentrations in the definition of the mass transfer  
 101 coefficient.

102 **III** Translation of the continuous experimental picture to numerical simu-  
 103 lations of a few unit cells, the issue of correspondence between space  
 104 averages (simulations [2]) and time averages (experiment).

105 In addition, at the end of the manuscript we present results of the depen-  
 106 dence of the volumetric mass transfer coefficient on the Peclet number that we  
 107 compare with analytical [15] and experimental correlations [7]. The thorough  
 108 determination of the mass transfer coefficient and associated Sherwood num-  
 109 ber as a function of other non-dimensional parameters such as gas holdup,  
 bubble/slug lengths, and the capillary number is left for future studies.

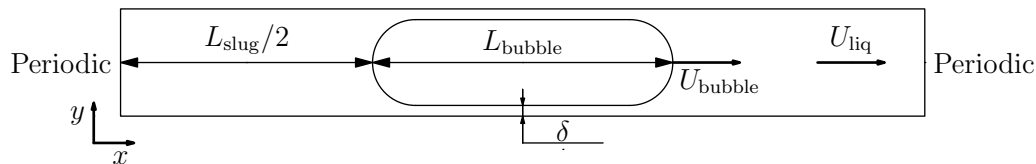


Figure 1: Simplified sketch of the bubble motion. Using periodic conditions for the velocity field is natural, but needs evaluation for mass transfer.

110  
 111 To establish numerical procedures we performed multiphase simulations  
 112 to extract bubble shapes [17, 13] for the range of capillary numbers  $Ca =$   
 113  $0.1 \div 1.0$ . For this range of capillary numbers we were able to capture the  
 114 bubble shape change and the change of hydrodynamic patterns. The mass  
 115 transfer simulations presented here were performed with various boundary  
 116 conditions (open, periodic) and with a few unit cells (1 to 10 unit cells). As  
 117 our numerical approach we take the lattice Boltzmann method, a relatively  
 118 new CFD competitor developed during last 20 years [18, 19, 20, 21]. This

119 method was successfully applied to simulate not only single phase hydro-  
 120 dynamic problems [22], but also multiphase flows [23, 24, 25], heat transfer  
 121 [26, 27], and ferrofluids [28, 29].

122 Mass transfer problems in the lattice Boltzmann framework were mainly  
 123 addressed in a series of works of Ginzburg and co-authors [30, 31, 32]. In con-  
 124 trast to these works whose focus was on simulating the advection-diffusion  
 125 equation via the lattice Boltzmann framework, we concentrate on the ap-  
 126 plication side. One should also mention the work of Yoshino and Inamuro  
 127 [33] about heat and mass transfers in porous media and the work of Derksen  
 128 [34] simulating lateral mixing in cross-channel flow. The last two works are  
 129 focused on problems of homogeneous nature and do not provide guidance as  
 130 to how to obtain the mass transfer coefficient for heterogeneous cases.

131 The paper is organized as follows. We start with definitions of the volu-  
 132 metric mass transfer coefficient and apply them to the bubble train flow to  
 133 derive expressions to connect the space- and time-averages. Then, the lattice  
 134 Boltzmann model used to simulate mass transfer is presented, followed by  
 135 benchmarks. Finally, numerical simulations of various boundary conditions  
 136 and simulations spanning a few unit cells for different hydrodynamic pat-  
 137 terns are presented to establish the procedure to determine the volumetric  
 138 mass transfer coefficient. The comparison with analytical correlations is also  
 139 presented.

## 140 2. Mass transfer definitions

By definition, the mass transfer coefficient from a surface with an imposed  
 constant concentration  $C_{\text{bubble}}$  is:

$$k_L = \frac{\dot{m}}{P\Delta C}, \quad \Delta C = C_{\text{bubble}} - C_{\text{medium}}, \quad (5)$$

141 where  $\dot{m}$  is the mass flux  $\left[\frac{kg}{s}\right]$ ,  $P$  is the area of the surface  $\left[m^2\right]$ , and  $\Delta C$  is  
 142 the concentration difference between the surface and the surrounding medium  
 143  $\left[\frac{kg}{m^3}\right]$ . Therefore,  $k_L$  has a dimension of  $\left[\frac{m}{s}\right]$ . Usually, the surrounding  
 144 medium concentration is taken at an infinite distance from the bubble. How-  
 145 ever, in the case of complicated geometries and non-homogeneous concen-  
 146 trations, the medium concentration can be the average concentration in the  
 147 domain or the flux-averaged concentration at the inlet or outlet, etc. Thus,  
 148 one needs to establish a clear definition of  $\Delta C$  to determine the volumetric

149 mass transfer coefficient in the case of complex geometries and non-trivial  
 150 hydrodynamic velocity patterns.

151 We first examine the definitions of mass transfer in the case of point  
 152 sources.

### 153 2.1. Point mass sources

154 In what follows we will present three approaches to calculate point mass  
 155 transfer coefficients (by point source we assume the source to have an in-  
 156 finitesimally small surface area  $P$ ):

1. Let us look at the infinitesimally small domain of volume  $A\Delta x$ , not moving and containing a point source. The concentration difference is  $\Delta C = C^* - C(t)$ , where  $C^*$  is the imposed point source concentration, and  $C(t)$  is the time-dependent concentration, which does not depend on the location due to the assumption of homogeneity. One can therefore write a time-dependent ordinary differential equation for the concentration in the domain:

$$\dot{m} = A\Delta x \frac{dC}{dt} = k_L P (C^* - C(t)), \quad (6)$$

with the initial condition  $C(0) = 0$ . The solution can be found as:

$$C(t) = C^* (1 - \exp(-k_L a t)), \quad (7)$$

where  $k_L a$  is the volumetric mass transfer coefficient defined as:

$$k_L a = k_L \frac{P}{A\Delta x} = k_L \frac{P}{V}, \quad (8)$$

157 where  $P$  is the source surface,  $V$  is the unit cell volume.

- 158 2. Let us predict mass transfer in a liquid moving with the velocity  $U$ , see  
 159 Fig. 2.

If one can assume that the point mass sources are distributed in the whole medium, the mass accumulated in the volume  $V = A\Delta x$  can be calculated as the difference of mass fluxes entering and leaving the domain  $U(C(x + \Delta x) - C(x))$ . The accumulated mass should be proportional to the mass transfer coefficient:

$$U(C(x + \Delta x) - C(x)) = k_L P (C^* - C(x)), \quad (9)$$



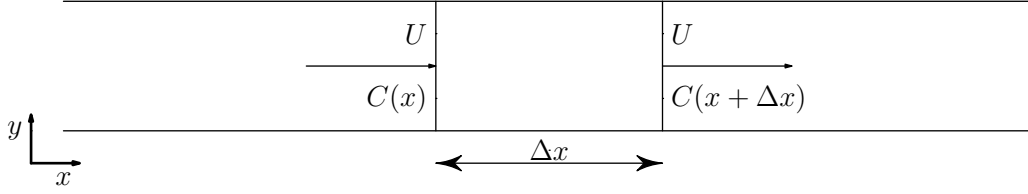


Figure 2: The mass transfer in a moving liquid.

giving the same solution but only in the spatial domain:

$$C(x) = C^* \left( 1 - \exp\left(-k_L a \frac{x}{U}\right) \right). \quad (10)$$

Note that the concentration  $C(x)$  does not depend on time.

3. If one transfers to the frame moving with the liquid velocity  $U$ , the situation will be the same as in the first case. One can connect time and space with the velocity  $U$  ( $t = \frac{x}{U}$ ) to obtain the same equation as in the case 2.

## 2.2. Bubble train

In the application to the bubble train flow it is useful to think of one bubble as a point source to be able to use the calculations presented above. For example, the expression (10) was used in experiments by Bercic and Pintar [4]. However, one should be accurate with the definition of velocities because two different phases co-exist in the bubble train flow. Usually, one can take the velocity  $U$  to be a bulk velocity or  $U = U_{\text{gas}} + U_{\text{liq}}$ , where  $U_{\text{gas}}$  and  $U_{\text{liq}}$  are liquid and gas superficial velocities, respectively.

With experimental measurements of concentration at different locations, the calculation of the mass transfer coefficient using the logarithmic function is straightforward. However, if one wants to analytically or numerically calculate the mass transfer coefficients, the situation is much more complicated because of the presence of two phases and complex bubble geometry. As was mentioned before, depending on the capillary number the velocity pattern and thus scalar mixing is different. Analytical approaches [15, 2] assume that the contributions from film and bubble caps can be calculated separately. Therefore no tracer from the film influences bubble caps diffusion. However, this assumption overpredicts mass transfer for a number of experiments [15]. This happens since some tracer concentration from the film is mixed with the slug and increases the overall concentration in the

185 slug, thereby decreasing the mass transfer from the bubble caps. Therefore,  
 186 the analytical estimates for the mass transfer coefficient calculation do not  
 187 account for mutual mass transfer from neighbouring bubbles.

188 Overall, mixing patterns of the film and liquid slugs are of great im-  
 189 portance for the estimation of mass transfer [7]. However, the assumptions  
 190 usually taken for mass transfer calculations are small capillary numbers and  
 191 certain mixing patterns such as to help to estimate the mass transfer using  
 192 the penetration theory of Higbie [16].

193 In comparison with analytical calculations and simplifications, the nu-  
 194 merical approach can take into account the complex mixing patterns and  
 195 geometries. However, there are challenges as how to mimic the continuous  
 196 picture where the medium is moving with bulk velocity  $U = U_{\text{gas}} + U_{\text{liq}}$  as  
 197 it is done in experiments. Thus, the questions indicated in Section 1 arise.  
 198 The next section gives more details about numerical simulations.

### 199 *2.3. Numerical simulations*

200 Ideally one wants to mimic the continuous picture as it is seen in ex-  
 201 periments. Thus, mass transfer simulations for a number of unit cells each  
 202 containing a bubble are needed. As was indicated above, there are two ap-  
 203 proaches towards it – either to simulate the bubble train and then to measure  
 204 concentration along the pipe, Eq. 10, or to transfer to the reference frame  
 205 moving with the bulk velocity  $U$  and conduct the same measurements. How-  
 206 ever, both methods require tracking of moving bubbles which is complicated  
 207 from the numerical point of view. Therefore, one needs to come up with a  
 208 simple and smaller domain for calculations of the mass transfer coefficient,  
 209 which closely mimics the continuous picture of a large number of separated  
 210 bubbles.

211 To avoid complications with moving grids, our approach is to simulate  
 212 mass transfer in a reference frame moving with the bubble. Therefore, one  
 213 needs to examine Eq. 10 more closely.

We perform simulations in the frame co-moving with the bubble in which  
 the bubble position stays constant. The bubble velocity  $U_{\text{bubble}}$  is different  
 from the bulk velocity  $U = U_{\text{gas}} + U_{\text{liq}}$ , and one thus needs to perform a  $x$

coordinate variable change:

$$\begin{aligned}
x(t) &= U_{\text{bubble}} t \\
\overline{C(x)} &= C^* \left( 1 - \exp \left( -k_L a \frac{x}{U_{\text{gas}} + U_{\text{liq}}} \right) \right) \\
\langle C(t) \rangle &= C^* \left( 1 - \exp \left( -k_L a t \frac{U_{\text{bubble}}}{U_{\text{gas}} + U_{\text{liq}}} \right) \right),
\end{aligned} \tag{11}$$

where  $\langle C(t) \rangle$  is the space-averaged characteristic concentration, and  $\overline{C(x)}$  is the time-averaged concentration at location  $x$ . One can make different choices for  $\langle C(t) \rangle$  such as the concentration averaged over the whole domain or inlet/outlet space-averaged concentrations used in works [2, 3]. The volumetric mass transfer coefficient can be obtained through the space-averaged concentration:

$$\begin{aligned}
k_L a t \frac{U_{\text{bubble}}}{U_{\text{gas}} + U_{\text{liq}}} &= \ln \frac{C^*}{C^* - \langle C(t) \rangle} \\
k_L a \frac{L_{\text{unit}}}{U_{\text{bubble}} + U_{\text{gas}}} &= \frac{L_{\text{unit}}}{U_{\text{bubble}} t} \ln \frac{C^*}{C^* - \langle C(t) \rangle},
\end{aligned} \tag{12}$$

where the parameter  $k_L a \frac{L_{\text{unit}}}{U_{\text{gas}} + U_{\text{liq}}}$  is non-dimensional. One can also measure the volumetric mass transfer coefficient from concentrations given at times  $t_1$  and  $t_2$ :

$$k_L a \frac{L_{\text{unit}}}{U_{\text{bubble}} + U_{\text{gas}}} = \frac{L_{\text{unit}}}{U_{\text{bubble}}(t_2 - t_1)} \ln \frac{C^* - \langle C(t_1) \rangle}{C^* - \langle C(t_2) \rangle}. \tag{13}$$

214 Expressions (11 - 13) are the cornerstones of the present work . Four possible  
215 scenarios of numerical simulations have been examined:

- 216 1. One unit cell is simulated with periodic boundary conditions, see Fig.
- 217 3. In this case no tracer leaves the domain similarly to the plug flow.
- 218 Though easier to implement, it gives rise to the criticism that the inlet
- 219 concentration is equal to the outlet one. As was discussed, in exper-
- 220 iments there is a concentration difference between the inlet and the
- 221 outlet, even for one unit cell.

In this case, the volumetric mass transfer coefficient is calculated by Eq. 12. The characteristic concentration  $\langle C(t) \rangle$  required for the volumetric

mass transfer coefficient is taken as the average concentration in the domain:

$$C(t) = \frac{\int_{liquid} C dV}{\int dV}. \quad (14)$$

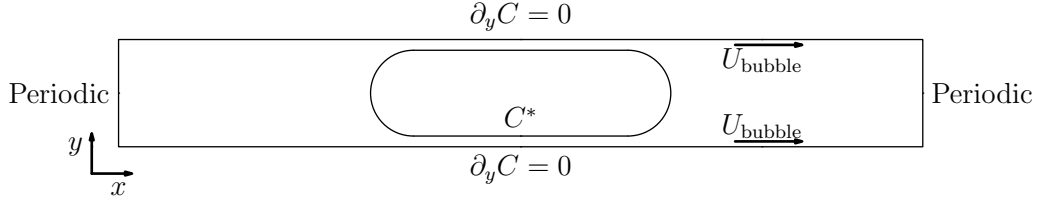


Figure 3: The two-dimensional benchmarks for the the mass transfer coefficient (bottom) for the bubble located near the entrance (top) and at the middle of the domain (bottom).

222

2. Periodic boundary conditions are applied as in the first case but the characteristic concentration is taken as the inlet/outlet flux-averaged concentration [2]:

$$\begin{aligned} \langle C_{inlet}(t) \rangle &= \frac{\int U(y)C(0, y, t)dy}{\int U(0, y)dy} \\ \langle C_{outlet}(t) \rangle &= \frac{\int U(y)C(L_{unit}, y, t)dy}{\int U(L_{unit}, y)dy} \\ C_{inlet}(\mathbf{x}, t) &= C_{outlet}(\mathbf{x}, t), \text{ due to periodicity.} \end{aligned} \quad (15)$$

223

224

225

226

The assumptions of this approach are that the concentration difference between the inlet/outlet- and the space-averaged over the whole unit cell is not significant. Thus, the tracer is assumed to be well mixed in the slug.

3. The approach of van Baten and Krishna [2], where periodic boundary conditions are used and the mass transfer coefficient is calculated as the gain of the mass in the system divided by the concentration difference multiplied by the surface area:

$$k_L a = \frac{\dot{m}}{P \Delta C} \frac{P}{V} = \frac{\dot{m}}{V(C^* - \langle C(t) \rangle)}, \quad (16)$$

where the mass flux in the domain can be calculated as:

$$\dot{m} = \frac{m_2 - m_1}{t_2 - t_1} = \frac{\int_{liq} C(\mathbf{x}, t_2) d\mathbf{x} - \int_{liq} C(\mathbf{x}, t_1) d\mathbf{x}}{t_2 - t_1}. \quad (17)$$

In the approach of van Baten and Krishna the inlet/outlet flux-averaged concentrations were taken as the characteristic concentration  $\langle C(t) \rangle$ .

4. Simulation of several unit cells, see Fig. 4. This situation corresponds to the head of the bubble train, after injection in the pipe and traveling along the channel. One can see that this situation best resembles the experimental picture, but also requires larger computational resources. By simulating a certain number of bubbles in the train head, the influence of the boundaries can be reduced. For example, left and right boundary conditions in this case are taken as open boundaries, i.e.  $\partial C / \partial x = 0$ . There is no ambiguity in the choice of the characteristic concentration. The average concentration of any unit cell far away from boundaries will be governed by Eq. 13.

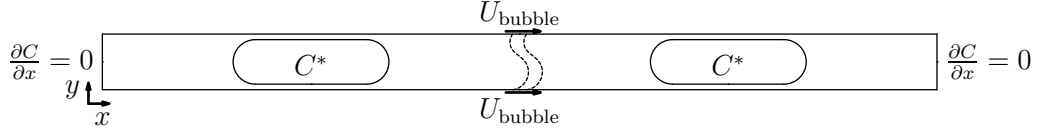


Figure 4: Benchmark for multiple unit cells.

One can notice that all examined cases are the extreme limits of one equation:

$$k_L a = \frac{\dot{m} - \int C_{\text{outlet}}(t) u(L_{\text{unit}}, y) dy + \int C_{\text{inlet}}(t) u(0, y) dy}{V \Delta C}, \quad (18)$$

where  $\Delta C = C^* - \langle C(t) \rangle$  with  $\langle C(t) \rangle$  taken to be the average concentration in the whole liquid domain,  $\dot{m}$  is the mass gain in the domain,  $\int C_{\text{inlet}} u(0, y) dy$  and  $\int C_{\text{outlet}} u(L_{\text{unit}}, y) dy$  are inlet/outlet mass fluxes. Eq. 18 describes the mass balance: whatever was generated by the bubble surface equals the domain mass change minus whatever left the domain plus whatever entered it.

Periodic boundary conditions are the extreme limiting case of Eq. 18:

$$\int C_{\text{outlet}}(t) u(L_{\text{unit}}, y) dy = \int C_{\text{inlet}}(t) u(0, y) dy.$$

Another limiting case (will be shown later) is when the mass accumulation rate equals zero, i.e.  $\dot{m} = 0$ . This situation corresponds to a simulation of a few unit cells with open boundary for flows with  $Ca > 0.7$ .

Before we examine all the test cases above, some lattice Boltzmann mass transfer benchmarks will be presented.

### 3. Validation

As was discussed earlier, analytical correlations for the mass transfer coefficient have been derived for a Taylor bubble train flow as two separate contributions: the mass transfer from two half circles and the mass transfer from the film. We will examine these mass transfer cases closely with the help of the lattice Boltzmann method and compare them against analytical solutions. The next sections will give a short introduction to the lattice Boltzmann method and present benchmark results.

#### 3.1. TRT D2Q9 model

The lattice Boltzmann equation (LBE) operates on a square/cubic grid representing the physical domain. It utilizes probability distribution functions (also known as particle populations) containing information about macroscopic variables, such as fluid density and momentum. LBE consists of two parts: a local collision step, and a propagation step which transports information from one node to another along directions specified by a discrete velocity set. The LBE is typically implemented as follows:

$$\begin{aligned} f_i^*(\mathbf{x}, t) &= f_i(\mathbf{x}, t) - \omega(f_i(\mathbf{x}, t) - eq_i(\mathbf{x}, t)), & \text{collision step} \\ f_i(\mathbf{x} + \mathbf{c}_i, t + 1) &= f_i^*(\mathbf{x}, t), & \text{propagation step,} \end{aligned} \quad (19)$$

where  $f_i$  is the probability distribution function in the direction  $\mathbf{c}_i$ ,  $eq_i$  is the equilibrium probability distribution function, and  $\omega$  is the relaxation parameter. The term  $-\omega(f_i - eq_i)$  is the so-called BGK collision operator [35]. However, the approach used here is the TRT (two-relaxation-times) collision operator [30, 32]. In comparison with the widely used BGK collision operator, the TRT collision operator has better accuracy for diffusion and convection fluxes, as well as a larger range of parameters where the scheme is stable.

The TRT collision operator [36] decomposes the populations and the equilibrium distribution into a symmetric and an antisymmetric part:

$$f_i^\pm = \frac{f_i \pm f_{\bar{i}}}{2}, \quad eq_i^\pm = \frac{eq_i \pm eq_{\bar{i}}}{2}, \quad (20)$$

where  $\bar{i}$  is the opposite direction to the  $i$ -th direction. The collision is performed with two independent relaxation rates for symmetric and antisymmetric modes:

$$\begin{aligned} f_i^*(\mathbf{x}, t) &= f_i(\mathbf{x}, t) - \omega_+(f_i^+ - eq_i^+) - \omega_-(f_i^- - eq_i^-) \\ f_i(\mathbf{x} + \mathbf{c}_i, t + 1) &= f_i^*(\mathbf{x}, t). \end{aligned} \quad (21)$$

267 Note that the TRT collision operator reduces to the BGK operator if  $\omega_+ =$   
 268  $\omega_-$ . In comparison with the BGK collision operator, the TRT collision oper-  
 269 ator has one additional degree of freedom. The TRT operator introduces the  
 270 following free parameter  $\Lambda = \left(\frac{1}{\omega_+} - \frac{1}{2}\right)\left(\frac{1}{\omega_-} - \frac{1}{2}\right)$ . This free parameter con-  
 271 trols the effective location of bounce-back walls [37], second-order accuracy  
 272 of boundary [36] and interface schemes [38], spatial accuracy [39, 40], con-  
 273 sistency [41] and, to some extent, stability [42, 43, 40]. In particular,  $\Lambda = \frac{1}{4}$   
 274 achieves the optimal stability for the isotropic advection-diffusion equation  
 275 [42].

The parameters  $\omega_+$ ,  $\omega_-$  and  $eq_i$  fully define the lattice Boltzmann procedure. The two-dimensional, nine-velocity LBM  $D2Q9$  we used in this work is defined on the set of lattice velocities with components:

$$\begin{aligned} c_{ix} &= \{0, 1, 0, -1, 0, 1, -1, -1, 1\}, \text{ for } i = 0 \dots 8 \\ c_{iy} &= \{0, 0, 1, 0, -1, 1, 1, -1, -1\}, \text{ for } i = 0 \dots 8. \end{aligned} \quad (22)$$

The equilibrium functions for the  $D2Q9$  TRT model are represented as [42]:

$$\begin{aligned} eq_i^+ &= eq_i^{(m)} + g^{(u)} eq_i^{(u)} \\ eq_i^{(m)} &= t_i^{(m)} c_e + eq_i^{(a)} \\ eq_i^{(u)} &= t_i^{(u)} \frac{u_x^2 + u_y^2}{2} + \frac{u_x^2 - u_y^2}{4} p_i^{(xx)} + g_{xy}^{(u)} \frac{u_x u_y}{4} p_i^{(xy)} \\ eq_i^{(a)} &= \frac{K_{xx} - K_{yy}}{4} p_i^{(xx)} + \frac{K_{xy}}{4} p_i^{(xy)} \\ eq_i^- &= t_i^{(a)} u_\alpha c_{i\alpha}, \end{aligned} \quad (23)$$

where  $K_{xx,yy,xy}$  are proportional to components of the diffusion tensor,  $c_e = \frac{K_{xx} + K_{yy}}{2}$ , parameters  $g^{(u)}$  and  $g_{xy}^{(u)}$  are either zero or one (see below), the tensor  $p_i^{(xx)} = c_{ix}^2 - c_{iy}^2$ , the tensor  $p_i^{(xy)} = c_{ix} c_{iy}$ , the weights  $t_i^{(u,m,a)}$  can be chosen based on stability criteria. The most commonly used set of weights, the

so-called “hydrodynamic“ weights, were chosen:

$$t_i^{(u)} = t_i^{(m)} = t_i^{(a)} = \left\{0, \frac{1}{3}, \frac{1}{3}, \frac{1}{3}, \frac{1}{3}, \frac{1}{12}, \frac{1}{12}, \frac{1}{12}, \frac{1}{12}\right\} \quad (24)$$

It can be shown through the Chapman-Enskog procedure [44], that the simple update rule with the equilibrium function presented above restores the anisotropic advection-diffusion equation:

$$\partial_t C + \partial_\alpha C u_\alpha = \partial_{\alpha\beta} D_{\alpha\beta} C, \quad (25)$$

where the concentration  $C = \sum_i f_i$ , and  $D_{\alpha\beta} = \left(\frac{1}{\omega_-} - \frac{1}{2}\right) K_{\alpha\beta}$  is the following diffusion tensor:

$$D_{\alpha\beta} = \begin{pmatrix} D_{xx} + \left(\frac{1}{\omega_-} - \frac{1}{2}\right)(g^{(u)} - 1)u_x^2 & D_{xy} + \left(\frac{1}{\omega_-} - \frac{1}{2}\right)(g_{xy}^{(u)} - 1)u_x u_y \\ D_{xy} + \left(\frac{1}{\omega_-} - \frac{1}{2}\right)(g_{xy}^{(u)} - 1)u_x u_y & D_{yy} + \left(\frac{1}{\omega_-} - \frac{1}{2}\right)(g^{(u)} - 1)u_y^2 \end{pmatrix} \quad (26)$$

276 We want to resolve the isotropic advection-diffusion equation,  $D = D_{xx} =$   
 277  $D_{yy}$  or  $K = K_{xx} = K_{yy}$ , with the non-diagonal diffusion tensor components  
 278 set to zero ( $D_{xy} = 0$ ). In contrast to the  $D2Q5$  model, with  $D2Q9$  it is possi-  
 279 ble to cancel the numerical diffusion by the proper choice of the equilibrium  
 280 functions, i.e.  $g_{xy}^{(u)} = g^{(u)} = 1$ . The particular choice of parameters used in  
 281 simulations is  $c_e = \frac{1}{3}$ ,  $\Lambda = \frac{1}{4}$ . Thus, the diffusion coefficient  $D$  is matched  
 282 through  $\omega_-$ , i.e.  $D = c_e \left(\frac{1}{\omega_-} - \frac{1}{2}\right) = \frac{1}{3} \left(\frac{1}{\omega_-} - \frac{1}{2}\right)$ . For the particular choice  
 283  $\Lambda = \frac{1}{4}$ ,  $\omega_+$  can be found easily as  $\omega_+ = 2 - \omega_-$ .

We validated two types of boundary conditions: Inamuro boundary conditions [33] and pressure anti bounce-back boundary conditions [37]. However, the simulation results are presented only for pressure anti bounce-back due to their ability to handle complex boundaries in a simple way:

$$f_{B,i}^* = -f_{F,\bar{i}}^* + 2eq^+(C^*, \mathbf{u}), \quad (27)$$

284 where  $C^*$  is the concentration to be imposed at the surface,  $\mathbf{u}$  is the surface  
 285 velocity,  $i$  is the direction number pointing to the domain located at the  
 286 boundary surface  $B$ ,  $\bar{i}$  is the direction number opposite to  $i$  and is located at  
 287 the fluid node  $F$  specifically so that node  $B$  is located at the location  $F + \mathbf{c}_i$ .

288 Note that the parameters of the lattice Boltzmann scheme are connected  
 289 with physical parameters only through non-dimensional numbers governing



the physics of the problem. In our case, this number is the Peclet number,  $Pe = \frac{U_{\text{bubble}} L}{D}$ . Therefore, one can choose any quantity, for example  $U_{\text{bubble}}$  in the lattice Boltzmann units as long as the Peclet number is matched in physical space and numerical simulations. The fact that  $U_{\text{bubble}}$  can be varied in certain ranges is extremely useful in the context of numerical simulations. This allows to increase the time step and decrease the computational demand (by an order of magnitude). This point will be used in simulations and covered later.

The next section will cover LBM benchmarks that resemble the mass transfer from a bubble (mass transfer to the liquid with the parabolic velocity profile and mass transfer from a cylinder).

### 3.2. The radial case

The case to be examined is the mass transfer from a circle with radius  $a$ , with the circle approximated as a stair-case. It can be described by the following system of equations:

$$\begin{aligned}\partial_t C(r, t) &= \frac{1}{r} \partial_r r \partial_r C(r, t) \\ C(a, t) &= C_0, \quad C(r, 0) = C_{\text{init}}\end{aligned}\tag{28}$$

The analytical solution is [45]:

$$\frac{C(r, t) - C_0}{C_{\text{init}} - C_0} = \sum_{n=1}^{\infty} \frac{2}{\mu_n J_1(\mu_n)} \exp\left(-\mu_n^2 \frac{Dt}{a^2}\right) J_0\left(\mu_n \frac{r}{a}\right),\tag{29}$$

where  $\mu_n$  is the  $n$ -th zero root of the 0th order Bessel polynomial  $J_0(\mu_n) = 0$ . Some of the corresponding roots are as follows:  $\mu_1 = 2.4048$ ,  $\mu_2 = 5.5201$ ,  $\mu_3 = 8.6537$ ,  $\mu_4 = 11.7915$ ,  $\mu_5 = 14.9309$ . By taking the initial concentration as 0, one obtains:

$$C(r, t) = C_0 \left( 1 - \sum_{n=1}^{\infty} \frac{2}{\mu_n J_1(\mu_n)} \exp\left(-\mu_n^2 \frac{Dt}{a^2}\right) J_0\left(\mu_n \frac{r}{a}\right) \right).\tag{30}$$

The solution depends only on the non-dimensional time:  $\tau = \frac{Dt}{a^2}$ . The domain size was  $129 \times 129$  with the circle radius  $a = 40$  lattice units. Some results for different diffusion coefficients are presented in Fig.5. The numerical simulations with the bounce-back boundary conditions are able to accurately reproduce the analytical results.

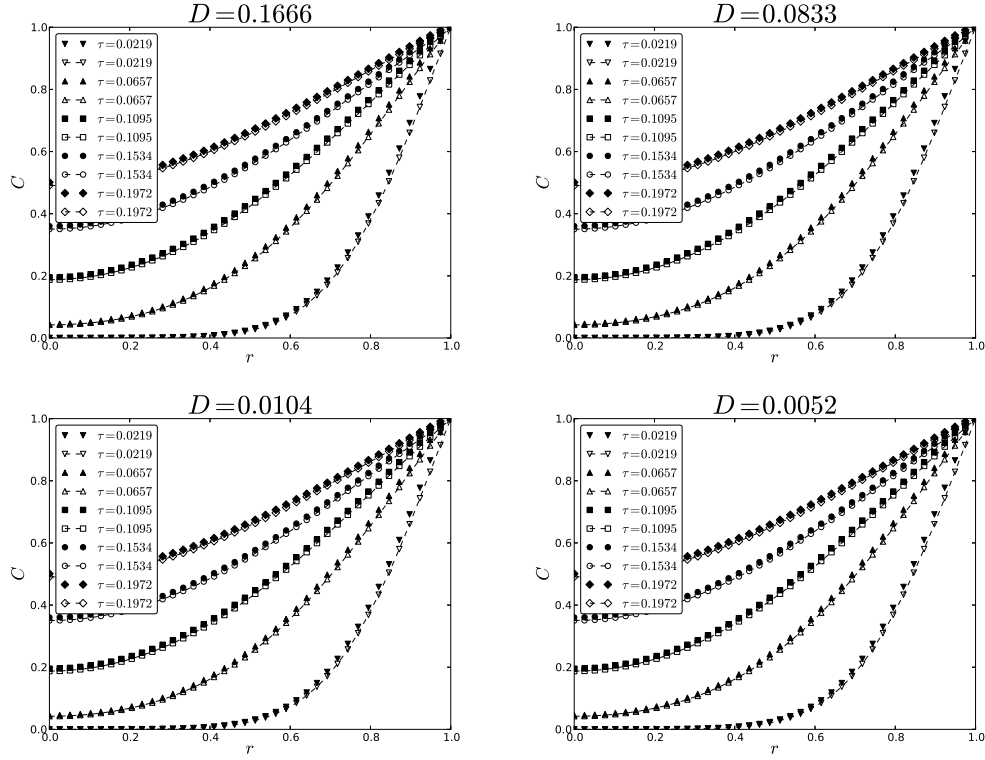


Figure 5: Profiles for different diffusion parameters varied with  $\omega_-$  (lines: Eq. 30, symbols: LB results). One can see that the diffusion from curved boundaries is captured accurately .  $r$  is the distance from the center.

### 307 3.3. Poiseuille velocity profile

The problem we want to address can be formulated through the following PDE:

$$\begin{aligned}
 \frac{\partial C}{\partial x} U(y) &= D \frac{\partial^2 C}{\partial y^2} \\
 C(0, y) &= 0, \quad C(x, \pm\delta) = C^*, \quad \frac{\partial C}{\partial y}(x, 0) = 0 \\
 U(y) &= U_0 \left( 1 - \left( \frac{y}{\delta} \right)^2 \right)
 \end{aligned} \tag{31}$$

The procedure to solve this problem is presented in Appendix A which yields the final solution as:

$$C = C^* - C^* \sum_{m=0} C_m e^{-m^4 \frac{x}{\delta} \frac{1}{Pe}} e^{-m^2 y^2 / (2\delta^2)} {}_1F_1\left(-\frac{m^2}{4} + \frac{1}{4}, \frac{1}{2}, m^2 \frac{y^2}{\delta^2}\right), \quad (32)$$

where coefficients  $C_m$  are taken from Eq. 48. The comparison between contours of analytical and simulation results is presented in Fig. 6. Parameters were taken as:  $D = 0.0185$ , the grid dimension is  $80 \times 1600$ . The centerline velocity is  $U_0 = 0.05$  which yields the Peclet number  $Pe = U_0 \delta / D = 108.108$ . The results are in good agreement. The simulations capture accurately the singular derivative for  $x = 0$ .

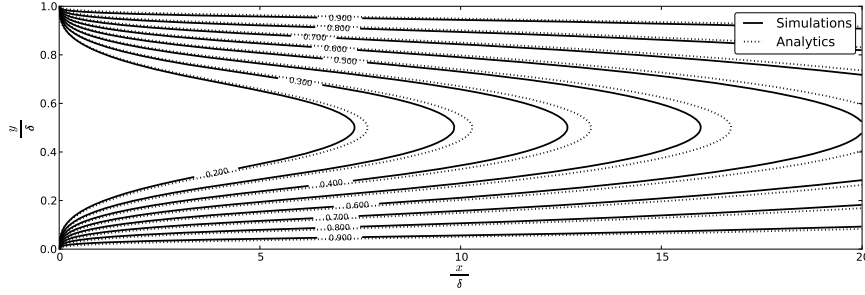


Figure 6: Comparison between the analytical concentration contours and simulations with pressure anti bounce-back conditions, Eq. 27. The simulation was done for  $D = 0.0185$  with a  $80 \times 1600$  grid. The centerline velocity is  $U_0 = 0.05$ , and the Peclet number is 108.108.

313

314 Now the LBM is validated against the benchmarks relevant for the flow  
315 around bubbles, one can examine the cases mentioned in Section 2.3 to cal-  
316 culate the volumetric mass transfer coefficient for Taylor bubble train flow.

#### 317 4. Numerical approach

318 A multiphase code was utilized to obtain the flow patterns and bubble  
319 shapes for different capillary numbers [17]. Five particular cases were cho-  
320 sen to be examined, their results are summarized in Table 1. Note that  
321 the velocities (LB system) in Table 1 are small. This means that to match  
322 large Peclet numbers,  $Pe = \frac{U_{\text{bubble}} L}{D}$ , usually used in experiments, one needs

$Ca$	$Re$	$U_{\text{bubble}}$	$\delta$	$\varepsilon_{\text{gas}}$	$U_{\text{liq}}$	$U_{\text{gas}}$	$L_{\text{bubble}}$	$L_{\text{slug}}$
0.097	1.656	0.0055	0.092	0.30	0.0046	0.0016	5.79	9.21
0.254	4.318	0.0143	0.132	0.28	0.0108	0.0041	6.12	8.88
0.526	8.938	0.0297	0.157	0.27	0.0209	0.0080	6.19	8.81
0.750	12.744	0.0424	0.167	0.25	0.0293	0.0107	5.96	9.04
1.040	17.665	0.0588	0.177	0.22	0.0397	0.0135	5.59	9.41

Table 1: Sample results with the binary liquid lattice Boltzmann model [17]. The following notations are used: the capillary number  $Ca = \frac{U_{\text{bubble}}L}{\rho\nu_{\text{liq}}}$ ,  $U_{\text{liq}}$  is the superficial liquid velocity,  $U_{\text{gas}}$  is the superficial gas velocity.  $\delta$  is the non-dimensional film thickness,  $L_{\text{bubble}}$  and  $L_{\text{slug}}$  are the non-dimensional bubble and slug lengths (defined in channel heights). The simulation sketch is presented in Fig. 1.

to decrease the diffusion coefficient  $D = \frac{1}{3}\left(\frac{1}{\omega_-} - \frac{1}{2}\right)$ . Thus, the parameter  $\omega_- \approx 0.5$ . However, for such values of  $\omega_-$  the stability of the lattice Boltzmann method drastically decreases [43]. On the other hand, one iteration in the lattice Boltzmann system corresponds to a physical time step  $\Delta t = U_{\text{bubble,LB}} \frac{\Delta x}{U_{\text{bubble,phys}}}$ . The iteration time is proportional to the velocity  $U_{\text{LB}}$  and the typical number of simulation steps to obtain the steady-state mass transfer coefficient for  $Ca < 0.2$  is of the order of a few million. Therefore, it is desirable to increase  $U_{\text{LB}}$  while maintaining the Peclet number. If one increases the velocity, then  $\omega_-$  increases as well, which impacts positively on the stability of the LBM.

Given all the considerations above, mass transfer simulations are performed as follows:

**Flow field** Given a capillary number  $Ca$ , one needs to obtain hydrodynamic fields around the bubble using the multiphase binary liquid lattice Boltzmann model according to our previous work [17]. Periodic boundary conditions were used in that work. The grid used was  $202 \times 3000$  which corresponds to the fluid domain of size  $200 \times 3000$ . That grid resolution was taken to ensure grid independency of the results [17]. Note that we do not approximate bubble shapes by correlations, but we directly resolve them by using the multiphase solver.

**Bubble reference frame** Once the hydrodynamics is solved, the mass transfer simulations are conducted in the reference frame moving with the bubble, where the bubble stands still and the liquid flows around the bubble. We impose a uniform and steady concentration on the surface

347 of the bubble with the anti bounce-back condition, Eq. 27.

348 **Velocity improvement** One can scale the velocity to perform faster sim-  
 349 ulations. However, before doing it one needs to improve the velocity  
 350 field. This issue arises because of the multiphase model used in the  
 351 flow simulations. The binary liquid lattice Boltzmann model is a dif-  
 352 fuse interface model where no clear boundary between gas and liquid  
 353 exists. We obtain the bubble shape by imposing a condition on the  
 354 order parameter field  $\phi$  with  $\phi \leq 0$  in the bubble [17]. The velocity of  
 355 the bubble is defined as the bubble tip velocity. Because of the square  
 356 grid, the shape of the bubble is determined within an accuracy of one  
 357 grid spacing. Thus, there is an error in the determination of the bubble  
 358 velocity. Though these errors are small, there is still a small non-zero  
 359 velocity component pointing into the bubble in some places, see Fig. 8  
 360 in [17] where some streamlines are penetrating the bubble surface. This  
 361 small velocity is amplified upon the velocity scaling and is inconsistent  
 362 with the advection-diffusion equation leading to instability after many  
 363 iterations.

364 Thus, before performing the mass transfer simulations an additional  
 365 single phase hydrodynamic simulation is performed. A free-surface  
 366 solver was developed in order to obtain a velocity field consistent with  
 367 the advection-diffusion equation. We take results from the multiphase  
 368 simulations, extract a bubble shape using the phase indicator  $\phi \leq 0$ ,  
 369 and approximate the bubble shape by the stair-case line with imposed  
 370 free-slip boundary condition on it. The obtained bubble velocity is  
 371 then imposed on the walls. This corresponds to conducting simula-  
 372 tions in the reference frame moving with the bubble. Appendix B cov-  
 373 ers the simple free-slip boundary condition implementation drastically  
 374 improving velocity patterns. The system is iterated until a steady state  
 375 is reached. Note, that these type of simulations are much faster than  
 376 the original multiphase simulations. As the output all the non-zero ve-  
 377 locity components perpendicular to the bubble surface are completely  
 378 eliminated. We compared original multiphase simulations with one-  
 379 component free-slip simulations. All quantities such as superficial slug  
 380 and liquid velocities are within 3% for the capillary number in the range  
 381  $0.05 \leq Ca \leq 1.0$ . One can see in Fig. 17 two streamline profiles for  
 382  $Ca = 0.097$  and  $Ca = 1.040$ .

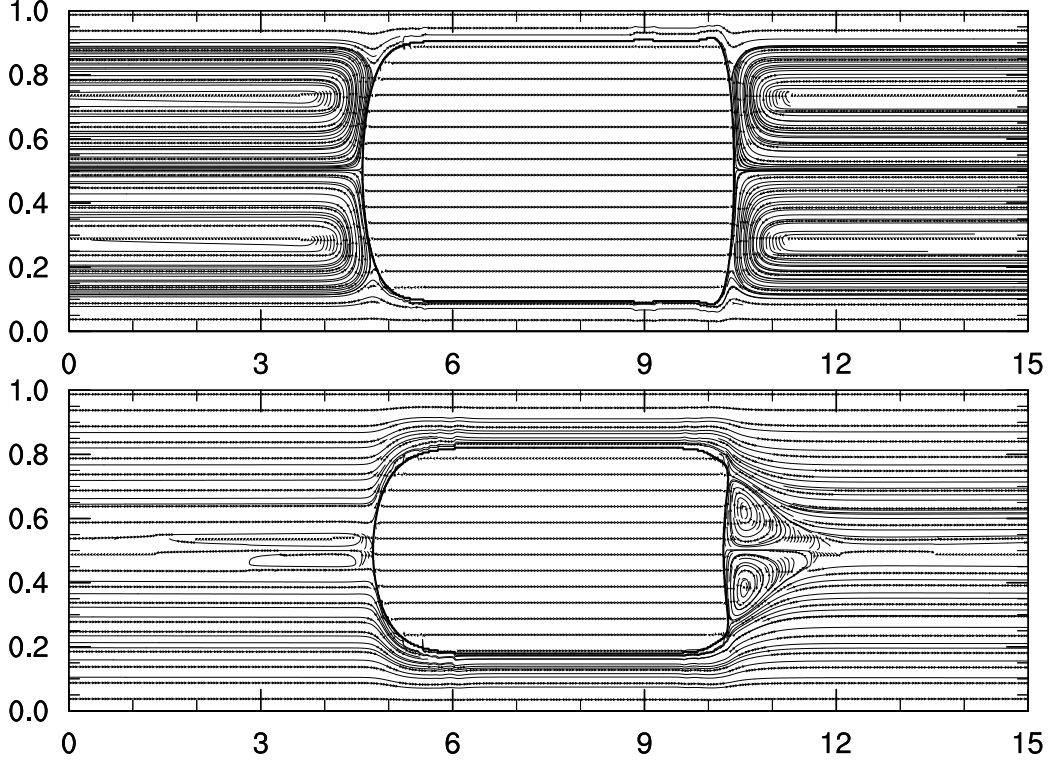


Figure 7: The streamline patterns produced by the free-surface flow solver with simplified approximation of the free-slip bubble surface, see Appendix B. Two completely different velocity patterns are obtained,  $Ca = 0.097$  (top) and  $Ca = 1.040$  (bottom).

383 **Mass transfer** After improved velocity profiles are obtained one can per-  
 384 form any mass transfer simulations with the various boundary condi-  
 385 tions as covered in Section 2.3. For this purpose one needs to match  
 386 the Peclet number  $Pe$  taken from experiments.

## 387 5. Results

388 This section covers simulation results. We first examine the possibility  
 389 to increase the fluid velocity while keeping the Peclet number the same.  
 390 After that the results for periodic boundary conditions for 5 capillary number  
 391 cases will be presented. Finally, we will examine many cell simulations for  
 392 two representative velocity patterns related to  $Ca = 0.0907$  and  $Ca = 1.04$   
 393 respectively (see Fig. 7).

### 394 5.1. Velocity scaling at constant Peclet number

This section addresses the process of significantly increasing the velocity magnitude while keeping dimensionless parameters the same to speed up simulations. This is especially important to be able to simulate a few unit cells in a reasonable time. For example, ten unit cell simulations require a grid of  $30000 \times 202$  nodes. Since the Peclet number is the only dimensionless quantity governing the advection-diffusion equation:

$$Pe = \frac{U_{\text{bubble}} N_y}{D}. \quad (33)$$

395 one needs to increase the diffusion coefficient when the velocity is increased.  
 396 Simulation runs were made with velocities 2, 4, 6, 8, 10, 15, 20, 40 times larger  
 397 than the original velocities. The velocities and their corresponding capillary  
 398 numbers are presented in Table 2. Periodic boundary conditions were used  
 399 and the mass transfer coefficient was calculated according to Eq. 4. Table  
 400 2 shows that the velocity limit for periodic boundary conditions is 0.1, so to  
 401 be on the safe side, velocities should not be scaled up beyond that value. For  
 402 example, in Table 2 for small capillary numbers ( $Ca < 0.2$ ) one can scale up  
 403 velocity significantly (20 – 40 times) to obtain a velocity around 0.2 where  
 404 simulations are still stable. However, for larger capillary numbers the scale  
 405 up is smaller (2 – 4 times), and the velocity for stable simulations is smaller  
 406 than 0.1. It gives us a preliminary idea to what extent one can scale periodic  
 407 mass transfer simulations. The concentration contour profiles corresponding  
 408 to Table 2 for different velocity scalings are presented in Fig. 8. One can  
 409 see an acceptable agreement between the cases with the same Peclet number  
 410 but different velocity scalings. Note, that the speedup can be up to 10 to 40  
 411 times.

### 412 5.2. Average concentration results

413 In this section we will examine the case where the volume averaged con-  
 414 centration over time is used as the characteristic concentration. To calculate  
 415 the volumetric mass transfer coefficient we used Eq. 12. Results for the  
 416 coefficient  $k_L a \frac{U_{\text{bubble}}}{U_{\text{gas}} + U_{\text{liq}}}$  are shown in Fig. 9 for different Peclet numbers and  
 417 velocity scalings indicated in Table 2. When the average concentration gets  
 418 close to  $C^* = 1$  then Eq. 12 gives inadequate results due to accuracy of  
 419 the logarithmic function evaluation. This is the reason that curves in Fig.  
 420 9 tend to shoot up for long times. Due to velocity scaling each simula-  
 421 tion has a different physical time step. Thus, we normalized time such that

Scale	$U_{bubble}$	$\omega_-$	Time Iterations	$C_{aver}$
-------	--------------	------------	-----------------	------------

$$Ca = 0.097, Pe = 1313$$

2	0.011	1.98	400000	0.318
4	0.023	1.96	200000	0.319
8	0.044	1.92	100000	0.320
10	0.055	1.90	80000	0.321
20	0.11	1.81	40000	0.324
40	0.22	1.66	20000	0.328

$$Ca = 0.254, Pe = 3414$$

2	0.0286	1.98	800000	0.6533
4	0.0572	1.96	400000	0.6591
8	0.1144	1.92	200000	0.6692
10	0.1430	1.90	160000	0.6734
20	0.2860	1.81	80000	0.6894

$$Ca = 0.526, Pe = 7092$$

2	0.0594	1.98	200000	0.3271
4	0.1188	1.96	100000	0.3315

$$Ca = 0.750, Pe = 10125$$

2	0.0848	1.98	200000	0.3489
---	--------	------	--------	--------

$$Ca = 1.040, Pe = 14041$$

2	0.1176	1.98	200000	0.3675
---	--------	------	--------	--------

Table 2: Indications of the achievable stable velocity  $U_{bubble}$  when one scales velocity. Since the physical time step represented by a single iteration of the simulation is directly proportional  $U_{bubble, LB}$ , scaling the velocity directly translates to an effective speed-up of the simulation. Note that time iterations indicated in the table correspond to the same moment in physical time. One can see that scaling produces adequate results when  $C_{aver}$  is compared. The contour profiles for all of these cases (capillary number  $Ca$  and all scales) are presented in Fig. 8.

422 it represents a number of unit cell lengths which the bubble will pass, i.e.  
423  $N_{cell\ units} = \frac{scale \cdot U_{bubble} \cdot N_{iter}}{L_{unit}}$ . Fig. 9 shows the volumetric mass transfer depen-



424 dency against the distance in unit cell length. One can see in Table 3 that for  
 425 different Peclet numbers different time (number of unit cells) is required to  
 426 achieve steady state. For example, for larger Peclet numbers fewer iterations  
 427 are required to achieve the steady state condition.

428 Overall one obtains steady state volumetric mass transfer coefficients for  
 429 periodic boundaries simulations if the following conditions are fulfilled:

- 430 **I** Scaling is performed as  $U_{max} = \text{scale} \cdot U_{\text{bubble}} \leq 0.1$ .
- 431 **II** The larger the Peclet number, the fewer iterations are required. One can  
 432 extrapolate data from Table 3, say  $L_{\text{steady}}$ , and estimate the number of  
 433 iterations to reach the steady-state as  $\text{scale} \cdot U_{\text{bubble}} \cdot N_{\text{iter}} \leq L_{\text{steady}}$ .

$Ca$	$Pe$	$L_{\text{steady}}/L_{\text{unit}}$	$k_L a \frac{L_{\text{unit}}}{U_{\text{bubble}} + U_{\text{gas}}}$
0.097	1313	7	0.21
0.254	3414	6	0.14
0.526	7092	3	0.095
0.750	10125	3	0.074
1.040	14041	2	0.0601

Table 3: The distance which a bubble propagates when the steady-state condition is achieved.

### 434 5.3. Periodic boundaries with the inlet/outlet characteristic concentration

435 The volumetric mass transfer coefficient was calculated using Eq. 12  
 436 with the characteristic concentration being the inlet/outlet flux averaged  
 437 concentration as used by van Baten and Krishna [2]. One can see in Fig.  
 438 10 that the calculated volumetric mass transfer behave differently from the  
 439 domain averaged volumetric mass transfer coefficient. For example, for small  
 440 capillary numbers, i.e.  $Ca = 0.097, 0.254, 0.526$  the values are overpredicted  
 441 ( $k_L a \frac{L_{\text{unit}}}{U_{\text{bubble}} + U_{\text{gas}}} = 0.3, 0.25, 0.1$ ). When the velocity pattern changes from  
 442 having a vortex in front of the bubble to not having it, i.e.  $Ca = 0.75, 1.04$   
 443 the calculated values are underpredicted compared to estimates based on  
 444 volume-averaged concentration, i.e.  $k_L a \frac{L_{\text{unit}}}{U_{\text{bubble}} + U_{\text{gas}}} = 0.06, 0.04$ . As we will  
 445 see later, the domain-averaged characteristic concentration produces proper  
 446 mass transfer coefficients.

#### 447 5.4. *Van Baten and Krishna formulation*

448 The van Baten and Krishna [2] formulation, Eq. 16, is calculated as the  
449 change of mass in the domain divided by the time difference. We examined  
450 two approaches: the characteristic concentration taken to be as the domain  
451 average and as the flux-averaged input/output concentration. The latter case  
452 corresponds to [2]. The results are presented in Fig. 11 for  $Ca = 0.097$  and  
453  $Ca = 1.04$ . One can see that the inlet/outlet flux averaged concentration is  
454 inconsistent. The reason that van Baten and Krishna [2] obtained the mass  
455 transfer coefficient close to the analytical estimation is that the liquid slug  
456 is well mixed ( $Ca < 0.1$  which is below the range studied here) so that the  
457 averaged concentration is close to the inlet/outlet concentration.

458 However, results for the domain-averaged concentration using the ap-  
459 proach of van Baten and Krishna are close to simulation results in Section  
460 5.2. Note that for  $Ca = 0.097$  the obtained mass transfer coefficient value is  
461 10% lower than the value in Section 5.2. However, as will be shown later the  
462 obtained volumetric mass transfer coefficient for  $Ca = 0.0097$  has the same  
463 value as for the simulations of a few unit cells. Therefore the approach of  
464 van Baten and Krishna [2] produces accurate results but if the characteris-  
465 tic concentration is the volume-averaged concentration (not the inlet/outlet  
466 flux-averaged concentration used in the original work). From the computa-  
467 tional point of view, it also requires the concentration fields in time and space  
468 to calculate the mass change in time and the averaged domain characteristic  
469 concentration.

#### 470 5.5. *Simulations for several unit cells*

471 In order to achieve independence from the boundary conditions and a  
472 closer match with the physical system being modelled, one can simulate  
473 several unit cells, corresponding to a head of the bubble train. If end effects  
474 are eliminated then the average domain characteristic should change in time  
475 according to Eq. 13. This eliminates the ambiguity inherent in choosing a  
476 definition of the characteristic concentration, it becomes the same domain-  
477 averaged concentration as the one measured in experiments.

478 This section studies the number of unit cells required for the volumetric  
479 mass transfer coefficient to be independent of the influence of boundaries.  
480 We chose two different velocity patterns (see Fig. 7 for  $Ca = 0.097$  and  
481  $Ca = 1.04$ ) to perform the simulations. For  $Ca = 0.097$  we performed  
482 simulations with 4, 6, 8, 10 cells, and for  $Ca = 1.040$  only with 4, 6, 8 cells.

483 We observed however that simulations with a domain length of 10 unit cells  
 484 produce the same results as those with 8 unit cells.

485 We keep velocity in the range  $0.05 - 0.1$  to avoid excessively long simula-  
 486 tion times. The number of steps for mass to pass through the whole domain  
 487 can be approximated as  $1.5 \frac{L_{\text{unit}}}{U_{\text{bubble}}}$ , which takes into account the bulk veloc-  
 488 ity. If  $U_{\text{bubble}}$  is taken as  $0.05$  then for the domain size  $L_{\text{unit}} = 3000$  one can  
 489 obtain the following number of iterations for the mass to cross the unit cell  
 490  $1.5 \frac{3000}{0.05} = 90000$ . Therefore,  $10^6$  iterations are enough for a system consisting  
 491 of 10 unit cells. For more accurate estimations of the number of time steps  
 492 depending on the Peclet number we refer to Section 5.1.

### 493 5.6. $Ca = 0.097$ results

There are two characteristics we want to track in the simulations: the  
 average concentration in the unit cell with time (see Eq. 13), and the accu-  
 mulated mass rate in the domain which takes into the account inlet/outlet  
 fluxes (see Eq. 18). The former resembles experiments: if one has a large  
 enough number of unit cells, then the averaged domain concentration should  
 change in time according to Eq. 13:

$$k_L a \frac{L_{\text{unit}}}{U_{\text{gas}} + U_{\text{liq}}} = \frac{L_{\text{unit}}}{U_{\text{bubble}}(t_2 - t_1)} \ln \left( \frac{C^* - \langle C(t_1) \rangle}{C^* - \langle C(t_2) \rangle} \right) \quad (34)$$

494 The non-dimensional volumetric mass transfer coefficient calculated based on  
 495 Eq. 34 (domain-averaged concentration change in time) is represented in Fig.  
 496 12 for different unit cells. One can see that mass transfer coefficient values are  
 497 the same as the mass flux concentration based on the van Baten and Krishna  
 498 formulation with the characteristic concentration being the domain-averaged  
 499 concentration (see Section 5.4). This demonstrates two things: the domain-  
 500 averaged concentration is the only choice for the characteristic concentration,  
 501 and periodic boundary conditions for one unit cell produce good results.

In comparison with periodic boundary conditions Eq. 18 allows to calcu-  
 late the mass transfer coefficient differently. Eq. 18 can be rewritten as:

$$k_L a \frac{L_{\text{unit}}}{U_{\text{bubble}} + U_{\text{gas}}} = \frac{L_{\text{unit}}}{U_{\text{gas}} + U_{\text{bubble}}} \frac{V \frac{\langle C(t_2) \rangle - \langle C(t_1) \rangle}{t_2 - t_1}}{- \int C_{\text{outlet}}(L_{\text{unit}}, y, t^*) u(L_{\text{unit}}, y) dy + \int C_{\text{inlet}}(0, y, t^*) u(0, y) dy \over V(C^* - \langle C(t^*) \rangle)}, \quad (35)$$

502 where  $t^*$  is the mean between  $t_1$  and  $t_2$ .

Fig. 13 shows average concentrations in different units and  $k_L a \frac{L_{\text{unit}}}{U_{\text{bubble}} + U_{\text{gas}}}$  based on Eq. 35 calculated for each unit for velocity scale 10 and 6 unit cells (all velocity scales produce the same results). It shows that the volumetric mass transfer coefficient is consistent for internal segments, i.e. unit cells numbers 2 – 4. The results for the volumetric mass transfer coefficient calculated by Eq. 18 for multiple unit cells are close (less than 10% deviation) to results for periodic boundary conditions in Section 5.2 . The same dependencies can be found for 8 and 10 unit cells simulations but we do not present them here. We also do not present 4 units cells simulation results which are highly influenced by entrance and exit effects.

The calculation of the volumetric mass transfer coefficient is more difficult using Eq. 35. However, it will be shown below that this equation can be significantly simplified in case of larger capillary numbers ( $Ca > 0.7$ ).

#### 5.7. $Ca = 1.040$ results

The same correlations were examined for a different velocity pattern at  $Ca = 1.040$ . The original Peclet number we started with is  $Pe = 14041$  (Table 2). To improve stability we changed the original Peclet number by increasing diffusion to  $Pe = 2644$ . The results with respect to the number of unit cells are the same as for  $Ca = 0.097$ : at least 6 unit cells are required to avoid the influence of inlet/outlet effects. Thus, only 6 unit cells results are presented in Fig. 14 which shows the average concentration for each unit cell. One can see that the average volume concentration for each unit cell converges to a constant value. Thus, all the mass generated by the bubble is transferred through the boundaries. This indicates that the liquid slug is unmixed since no concentration travels back to inlet with the vortex and increases the average concentration in each unit cell. Note that the periodic boundary conditions cannot show whether the liquid slug is mixed or not due to the fact that the averaged domain concentration always increases in time. Thus, the volumetric mass transfer coefficient  $k_L a \frac{L_{\text{unit}}}{U_{\text{bubble}} + U_{\text{gas}}}$  can be calculated according to the definition, Eq. 18:

$$k_L a = \frac{\dot{m} - \int C_{\text{outlet}}(y)u(L_{\text{unit}}, y)dy + \int C_{\text{inlet}}(y)u(L_{\text{unit}}, y)dy}{V(C^* - \langle C(t) \rangle)}, \quad (36)$$

where  $V$  is the unit cell volume. There is no accumulated mass in the domain, so  $\dot{m} = 0$ . Like periodic boundary conditions, this case is another extreme limit of Eq. 18. Note that to calculate the volumetric mass transfer coefficient

one needs only the spatial information and does not require the knowledge of how the averaged concentration changes in time, which significantly lowers storage requirements for the simulations with  $Ca > 0.7$  where there is no vortex in the liquid slug.

Fig. 15 (bottom) shows the volumetric mass transfer coefficient based on spatial calculations of inlet/outlet concentrations. One can see that the volumetric mass transfer coefficient is close to the calculated volumetric mass transfer coefficient using the time averaged approach and periodic boundaries one unit cell simulations (presented in the same figure for comparison). Note that results for approaches which incorporate the volume-averaged characteristic concentration either for one cell or a few unit cells coincide. Therefore, for certain hydrodynamic patterns ( $Ca > 0.7$ ), one can easily convert time domain to spatial domain calculations using simulations of several unit cells.

#### 5.8. Comparison of experimental and analytical correlations

While the goal of this paper is not to compare simulation results with the experimental measurements, we felt that a short note about such comparison will be beneficial. Unfortunately, to the authors' knowledge, there are no reported experimental results measuring the mass flux for bubbles flowing between parallel plates. However, an interesting correlation for the mass transfer volumetric coefficient was presented by Yue et al. [7] for three-dimensional microchannel geometries:

$$k_L a = \frac{2}{d_h} \left( \frac{DU_{\text{bubble}}}{L_{\text{bubble}} + L_{\text{slug}}} \right)^{0.5} \left( \frac{L_{\text{bubble}}}{L_{\text{bubble}} + L_{\text{slug}}} \right)^{0.3}$$

$$k_L a \frac{L_{\text{unit}}}{U_{\text{gas}} + U_{\text{liq}}} = 2 \frac{L_{\text{unit}}}{d_h} \left( \frac{D}{L_{\text{unit}}(U_{\text{bubble}} + U_{\text{gas}})} \frac{U_{\text{bubble}}}{U_{\text{gas}} + U_{\text{liq}}} \right)^{0.5} \left( \frac{L_{\text{bubble}}}{L_{\text{bubble}} + L_{\text{slug}}} \right)^{0.3} \propto Pe^{-\frac{1}{2}} \quad (37)$$

One can see that the volumetric mass transfer correlation should be approximately proportional to  $Pe^{-0.5}$ . One can also use analytical estimates of the volumetric mass transfer coefficient calculated using the Higbie penetration theory [16]. One can derive the analytical expression for the mass transfer for bubble train flow between parallel plates by following the works [15, 2]:

$$k_L a \frac{L_{\text{unit}}}{U_{\text{bubble}} + U_{\text{gas}}} = \frac{L_{\text{unit}}}{U_{\text{gas}} + U_{\text{liq}}} \left( 4\sqrt{DU_{\text{bubble}}\pi} \frac{\sqrt{L_{\text{bubble}} - H(1 - 2\delta)}}{L_{\text{unit}}H} + 2\sqrt{2}\sqrt{DU_{\text{bubble}}} \frac{\sqrt{H(1 - 2\delta)}}{L_{\text{unit}}H} \right), \quad (38)$$

535 where  $H$  is the channel height, and  $\delta$  is the non-dimensional film thickness  
536 (in channel heights).

537 Fig. 16 shows a comparison between the correlation by Yue et al. [7], the  
538 analytical expression, Eq. 38, and the current simulation results presented  
539 in Table 3. The coefficients are close to each other, especially given that  
540 the correlation by Yue et al. [7] is for three-dimensional cases. The fitting  
541 procedure for this work results showed that the power of the Peclet number  
542 dependence is  $-0.50038$  which is close to the theoretical value  $-0.5$ . The  
543 fitting curve is  $7.745Pe^{-0.50038}$ .

## 544 6. Summary

545 This work examines a way to calculate the volumetric mass transfer coef-  
546 ficient of Taylor/Batchelor bubble train flow in the framework of the lattice  
547 Boltzmann method. Overall, the easiest recipe is to perform simulations with  
548 periodic boundary conditions and calculate the volumetric mass transfer co-  
549 efficient based on the domain-averaged concentration through any formula-  
550 tion (van Baten and Krishna, periodic boundary conditions, simulations of  
551 several unit cells) as they produce consistent results. The best accuracy is  
552 achieved with formulations based on the mass difference or on the averaged  
553 domain concentrations taken in different times, Eq. 13. Eq. 11 gives a  
554 slightly overestimated volumetric mass transfer coefficients (less than 10%).  
555 The original formulation of van Baten and Krishna [2] is inconsistent if one  
556 takes the inlet/outlet flux-averaged concentration to be the characteristic  
557 concentration. Simulations of several unit cells are harder to perform, but  
558 they indicate how well the liquid slug is mixed. For velocity patterns related  
559 to  $Ca \geq 0.7$  simulations with a few unit cells allow to calculate the volu-  
560 metric mass transfer coefficient based on the spatial location only, without  
561 requiring the time snapshots of domain concentration values used in all other  
562 approaches. Finally, a sample of results was compared with the experimental  
563 correlation of Yue et al. [7] and shown to be consistent.

## 564 7. Acknowledgements

565 M.J. acknowledges a scholarship from the TWING project co-financed  
566 by the European Social Fund. A.K. wants to thank Schlumberger for their  
567 financial support.

### 568 A. Mass transfer for planar Poiseuille flow

Close to the previous example but with a different velocity profile, the problem can be formulated through the following PDE:

$$\begin{aligned}\frac{\partial C}{\partial x}U(y) &= D\frac{\partial^2 C}{\partial y^2} \\ C(0, y) &= 0, \quad C(x, \pm\delta) = C^*, \quad \frac{\partial C}{\partial y}(x, 0) = 0 \\ U(y) &= U_0\left(1 - \left(\frac{y}{\delta}\right)^2\right)\end{aligned}\tag{39}$$

The following substitution simplifies the form of equations:

$$\begin{aligned}\zeta &= \frac{x}{\delta} \frac{D}{U_0\delta} = \frac{1}{Pe} \frac{x}{\delta} \\ \xi &= \frac{y}{\delta}.\end{aligned}\tag{40}$$

Then the following equation can be obtained:

$$\begin{aligned}\frac{\partial \Theta}{\partial \zeta}(1 - \xi^2) &= \frac{\partial^2 \Theta}{\partial \xi^2} \\ \Theta(\zeta, \xi) &= C - C^* \quad \Theta(0, \xi) = -C^* \quad \Theta(0, \pm 1) = 0\end{aligned}\tag{41}$$

After separation of variables,  $\Theta(\zeta, \xi) = X(\zeta)Y(\xi)$  one can come up with two equations:

$$\begin{aligned}\frac{dX(\zeta)}{d\zeta} + m^4 X(\zeta) &= 0 \\ \frac{d^2 Y(\xi)}{d\xi^2} + m^4(1 - \xi^2)Y(\xi) &= 0\end{aligned}\tag{42}$$

The first equation has a solution:

$$X(\zeta) = \exp(-m^4 \zeta)\tag{43}$$

The second equation can be simplified after substitution  $\bar{\xi} = m\sqrt{2}\xi$  to the standard equation:

$$Y'' - \left(\frac{1}{4}\bar{\xi}^2 + a\right)Y = 0,\tag{44}$$

where  $Y' = dY/d\bar{\xi}$ , and  $a = -m^2/2$ . The equation above has two solutions via parabolic cylinder functions or through the confluent hypergeometric function [46]:

$$\begin{aligned} Y_1 &= e^{-\bar{\xi}^2/4} {}_1F_1\left(\frac{a}{2} + \frac{1}{4}, \frac{1}{2}, \frac{\bar{\xi}^2}{2}\right) \\ Y_2 &= e^{-\bar{\xi}^2/4} {}_1F_1\left(\frac{a}{2} + \frac{3}{4}, \frac{3}{2}, \frac{\bar{\xi}^2}{2}\right) \end{aligned} \quad (45)$$

Taking symmetry conditions into consideration by leaving only the even solution, Eq. 42 has the following solution:

$$Y_m = C_m e^{-m^2 \xi^2/2} {}_1F_1\left(-\frac{m^2}{4} + \frac{1}{4}, \frac{1}{2}, m^2 \xi^2\right) \quad (46)$$

To satisfy the boundary condition we need to find zeros of the hypergeometric function, i.e.  ${}_1F_1\left(-\frac{m^2}{4} + \frac{1}{4}, \frac{1}{2}, m^2\right) = 0$ . First ten eigenvalues can be found using numerical methods: 1.2967, 2.3811, 3.1093, 3.6969, 4.2032, 4.6548, 5.0662, 5.4467, 5.8023, 6.1373. One needs to satisfy one more condition to obtain coefficients  $C_m$ :

$$-C^* = \sum_m C_m e^{-m^2 \xi^2/2} {}_1F_1\left(-\frac{m^2}{4} + \frac{1}{4}, \frac{1}{2}, m^2 \xi^2\right) \quad (47)$$

One can multiply both parts on  $(1 - \xi^2) {}_1F_1\left(-\frac{m^2}{4} + \frac{1}{4}, \frac{1}{2}, m^2 \xi^2\right)$  and through orthogonality (Stourm-Liouville theorem) obtain coefficients:

$$C_m = -C^* \frac{\int_{\xi=0}^1 (1 - x^2) e^{-m^2 \xi^2/2} {}_1F_1\left(-\frac{m^2}{4} + \frac{1}{4}, \frac{1}{2}, m^2 \xi^2\right) d\xi}{\int_{\xi=0}^1 (1 - \xi^2) e^{-m^2 \xi^2/2} {}_1F_1\left(-\frac{m^2}{4} + \frac{1}{4}, \frac{1}{2}, m^2 \xi^2\right)^2 d\xi} \quad (48)$$

Therefore the complete solution can be written as:

$$C = C^* - C^* \sum_{m=0} C_m e^{-m^4 \frac{x}{\delta} \frac{1}{Pe}} e^{-m^2 y^2 / (2\delta^2)} {}_1F_1\left(-\frac{m^2}{4} + \frac{1}{4}, \frac{1}{2}, m^2 \frac{y^2}{\delta^2}\right), \quad (49)$$

569 where coefficients  $C_m$  are taken from Eq. 48. For the case  $C^*$ , the first ten  
570 coefficients are: 1.2008,  $-0.2991$ ,  $0.1608$ ,  $-0.1074$ ,  $0.0796$ ,  $-0.0627$ ,  $0.0515$ ,  
571  $-0.0435$ ,  $0.0375$ ,  $-0.0329$ .



## 572 B. Free surface boundary conditions

573 There are a few implementations of free boundary conditions [47, 48].  
 574 However, we developed the easy solver to impose the free surface boundary  
 575 conditions at the complicated surface of the bubble. The reason is to impose  
 576 the symmetric boundary conditions. Because the boundary is a staircase  
 577 approximation, one can find the normal to the boundary which is always  
 578 located by the angle of multiple of 45 degrees, see Fig. 17. This can be  
 579 done automatically by the simple coding. Imposing the symmetric boundary  
 580 conditions requires  $U_{n,F}=U_{n,B}$  and  $U_{\tau,F} = U_{\tau,B}$ . We can copy populations  
 581 in the certain order to do it, for example  $f_{B,i} = f_{F,\bar{i}}$ , where  $c_i$  and  $c_{\bar{i}}$  are  
 582 complementary directions, where  $c_{i,n} = -c_{\bar{i},n}$  and  $c_{i,\tau} = c_{\bar{i},\tau}$ , where  $c_{i,n} =$   
 583  $(\mathbf{c}_i \cdot \mathbf{n})\mathbf{n}$  and  $c_{i,\tau} = \mathbf{c}_i - (\mathbf{c}_i \cdot \mathbf{n})\mathbf{n}$ .

## 584 References

- 585 [1] M.D. Giavedoni and F.A. Saita. The axisymmetric and plane cases of  
 586 a gas phase steadily displacing a Newtonian liquid - A simultaneous  
 587 solution of the governing equations. *Phys. Fluids*, 9(8):2420–2428, 1997.
- 588 [2] J.M. van Baten and R. Krishna. CFD simulations of mass transfer from  
 589 Taylor bubbles rising in circular capillaries. *Chem. Eng. Sc.*, 59:2535–  
 590 2545, 2004.
- 591 [3] M.T. Kreutzer, F. Kapteijn, J.A. Moulijn, and J.J. Heiszwolf. Multi-  
 592 phase monolith reactors: Chemical reaction engineering of segmented  
 593 flow in microchannels. *Chem. Eng. Sci.*, 60:5895–5916, 2005.
- 594 [4] G. Bercic and A. Pintar. The role of gas bubbles and liquid slug lengths  
 595 on mass transport in the Taylor flow through capillaries. *Chem. Eng.*  
 596 *Sci.*, 52(21-22):3709–3719, 1997.
- 597 [5] F.P. Bretherton. The motion of long bubbles in tubes. *J Fluid Mech.*,  
 598 10(2):166–188, 1960.
- 599 [6] G.I. Taylor. Deposition of a viscous fluid on the wall of a tube. *J. Fluid*  
 600 *Mech.*, 10:161–165, 1961.
- 601 [7] J. Yue, L. Luo, Y. Gonthier, G. Chen, and Q. Yuan. An experimen-  
 602 tal study of air-water Taylor flow and mass transfer inside square mi-  
 603 crochannels. *Chem. Eng. Sci.*, 64:3697–3708, 2009.

- 604 [8] R. Gupta, D.F. Fletcher, and B.S. Haynes. Taylor Flow in Microchan-  
605 nels: A Review of Experimental and Computational Work. *J. Comput.*  
606 *Multiphase Flows*, 2:1–32, 2010.
- 607 [9] M.T. Kreutzer, M.G. van der Eijnded, F. Kapteijn, J.A. Moulijn, and  
608 J.J. Heiszwolf. The pressure drop experiment to determine slug lengths  
609 in mulitphase monoliths. *Catalysis Today*, 105:667–672, 2005.
- 610 [10] W.B. Kolb and R.L. Cerro. Film Flow in the Space between a Circular  
611 Bubble and a Square tube. *J. Coll. Int. Sci.*, 159:302–311, 1993.
- 612 [11] T.C. Thulasidas, M.A. Abraham, and R.L. Cerro. Bubble-train flow in  
613 capillaries of circular and square cross section. *Chem. Eng. Sci.*, 50(2):  
614 183–199, 1995.
- 615 [12] D. Liu and S. Wang. Hydrodynamics of Taylor flow in noncircular  
616 capillaries. *Chem. Eng. and Processing*, 47:2098–2106, 2008.
- 617 [13] A. Kuzmin, M. Januszewski, D. Eskin, F. Mostowfi, and J. Derksen.  
618 Three-dimensional binary-liquid lattice boltzmann simulation of mi-  
619 crochannels with rectangular cross sections. *Chem. Eng. J.*, 178:306–  
620 316, 2011.
- 621 [14] A.L. Hazel and M. Heil. The steady propagation of a semi-infinite bubble  
622 into a tube of elliptical or rectangular cross-section. *J. Fluid Mech.*, 470:  
623 91–114, 2002.
- 624 [15] S. Irandoust and B. Ertle, S. adn Andersson. Gas-Liquid Mass Transfer  
625 in Taylor Flow Through a Capillary. *Canadian J. Chem. Eng.*, 70:115–  
626 119, 1992.
- 627 [16] R. Higbie. The rate of absorption of a pure gas into a still liquid during  
628 short periods of exposure. *Trans. Amer. Inst. Chem. Eng.*, 31:365–389,  
629 1935.
- 630 [17] A. Kuzmin, M. Januszewski, D. Eskin, F. Mostowfi, and J. Derksen.  
631 Simulations of gravity-driven flow of binary liquids in microchannels.  
632 *Chem. Eng. J.*, 171(2):646–654, 2011.
- 633 [18] U. Frisch, D. d’Humieres, B. Hasslacher, P. Lallemand, Y. Pomeau, and  
634 J.-P. Rivet. Lattice gas hydrodynamics in two and three dimensions.  
635 *Complex Systems*, 1:649–707, 1987.

- 636 [19] G.R. McNamara and G. Zanetti. Use of the Boltzmann Equation to  
637 Simulate Lattice-Gas Automata. *Phys. Rev. Lett.*, 61(20):2332–2335,  
638 1988.
- 639 [20] F.J. Higuera and J. Jimenez. Boltzmann Approach to Lattice Gas Sim-  
640 ulations. *Europhys. Lett.*, 9(7):663–668, 1989.
- 641 [21] F.J. Higuera, S. Succi, and R. Benzi. Lattice gas dynamics with en-  
642 hanced collisions. *Europhys. Lett.*, 9(4):345–349, 1989.
- 643 [22] D. Yu, R. Mei, L.-S. Luo, and W. Shyy. Viscous flow computations  
644 with the method of lattice Boltzmann equation. *Progress in Aerospace*  
645 *Sciences*, 39:329–367, 2003.
- 646 [23] X. Shan and H. Chen. Simulation of nonideal gases and gas-liquid phase  
647 transitions by the lattice Boltzmann Equation. *Phys. Rev. E*, 49(4):  
648 2941–2948, 1994.
- 649 [24] M.R. Swift, W.R. Osborn, and J.M. Yeomans. Lattice Boltzmann Sim-  
650 ulation of Nonideal Fluids. *Phys. Rev. Lett.*, 75(5):831–834, 1995.
- 651 [25] A.K. Gunstensen, D.H. Rothman, S. Zaleski, and G. Zanetti. Lattice  
652 Boltzmann model of immiscible fluids. *Phys. Rev. A*, 43(8):4320–4327,  
653 1991.
- 654 [26] P. Yuan and L. Schaefer. A Thermal Lattice Boltzmann Two-Phase  
655 Flow Model and Its Application to Heat Transfer Problems -Part 2.  
656 Integration and Validation. *J. Fluids Eng.*, 128:151–156, 2006.
- 657 [27] R. Zhang and H. Chen. Lattice Boltzmann method for simulations of  
658 liquid-vapor thermal flows. *Phys. Rev. E*, 67(066711):1–6, 2003.
- 659 [28] P.J. Dellar. Lattice Kinetic Formulation for Ferrofluids. *J. Stat. Phys.*,  
660 121:105–118, 2005.
- 661 [29] G. Falcucci, G. Chiatti, S. Succi, A.A. Mohamad, and A. Kuzmin. Rup-  
662 ture of a ferrofluid droplet in external magnetic fields using a single-  
663 component lattice Boltzmann model for nonideal fluids. *Phys. Rev. E*,  
664 79(056706):1–5, 2009.

- 665 [30] I. Ginzburg. Equilibrium-type and link-type lattice Boltzmann models  
666 for generic advection and anisotropic-dispersion equation. *Adv. Wat.*  
667 *Res.*, 28:1171–1195, 2005.
- 668 [31] I. Ginzburg. Generic boundary conditions for lattice Boltzmann models  
669 and their application to advection and anisotropic dispersion equations.  
670 *Adv. Wat. Res.*, 28:1196–1216, 2005.
- 671 [32] I. Ginzburg. Variably saturated flow described with the anisotropic  
672 Lattice Boltzmann methods. *Comput. Fluids*, 35:831–848, 2006.
- 673 [33] M. Yoshino and T. Inamuro. Lattice Boltzmann simulations for flow and  
674 heat/mass transfer problems in a three-dimensional porous structure.  
675 *Int. J. Num. Meth. Fluids*, 43:183–198, 2003.
- 676 [34] J.J. Derksen. Simulations of lateral mixing in cross-channel flow. *Com-*  
677 *put. Fluids*, 39:1058–1069, 2010.
- 678 [35] P. L. Bhatnagar, E. P. Gross, and M. Krook. A Model for Collision  
679 Processes in Gases. I. Small Amplitude Processes in Charged and Neutral  
680 One-Component Systems. *Phys. Rev.*, 94(3):511–525, 1954.
- 681 [36] I. Ginzburg, F. Verhaeghe, and D. d’Humières. Two-relaxation-time  
682 Lattice Boltzmann scheme: about parametrization, velocity, pressure  
683 and mixed boundary conditions. *Commun. Comput. Phys.*, 3(2):427–  
684 478, 2008.
- 685 [37] I. Ginzburg and D. d’Humières. Multireflection boundary conditions for  
686 lattice Boltzmann models. *Phys. Rev. E*, 68(066614):1–30, 2003.
- 687 [38] I. Ginzburg. Lattice Boltzmann modeling with discontinuous collision  
688 components: Hydrodynamic and Advection-Diffusion Equations. *J.*  
689 *Stat. Phys.*, 126(1):157–206, 2007.
- 690 [39] D. d’Humières and I. Ginzburg. Viscosity independent numerical errors  
691 for Lattice Boltzmann models: From recurrence equations to ”magic”  
692 collision numbers. *Comp. Math. Appl.*, 58(5):823–840, 2009.
- 693 [40] B. Servan-Camas and F. T.-C. Tsai. Lattice Boltzmann method with two  
694 relaxation times for advection-diffusion equation: Third order analysis  
695 and stability analysis. *Adv. Wat. Res.*, 31:1113–1126, 2008.

- 696 [41] I. Ginzburg. Consistent Lattice Boltzmann schemes for the Brinkman  
697 model of porous flow and infinite Chapman-Enskog expansion. *Phys.*  
698 *Rev. E*, 77(066704):1–12, 2008.
- 699 [42] I. Ginzburg, D. D’Humières, and A. Kuzmin. Optimal Stability of  
700 Advection-Diffusion Lattice Boltzmann Models with Two Relaxation  
701 Times for Positive/Negative Equilibrium. *J. Stat. Phys.*, 139(6):1090–  
702 1143, 2009.
- 703 [43] A. Kuzmin, I. Ginzburg, and A.A. Mohamad. The role of the kinetic pa-  
704 rameter in the stability of two-relaxation-time advection-diffusion lattice  
705 Boltzmann schemes. *Comp. Math. Appl.*, 61:3417–3442, 2011.
- 706 [44] S. Chapman and T.G. Cowling. *The mathematical theory of non-uniform*  
707 *gases*. Cambridge University Press, Cambridge, third edition, 1995.
- 708 [45] A.D. Polyinin, A.M. Kutepov, A.V. Vyazmin, and D.A. Kazenin. *Hy-*  
709 *drodynamics, Mass and Heat Transfer in Chemical Engineering*. Taylor  
710 and Francis, 2002.
- 711 [46] M. Abramowitz and I. Stegun, editors. *Handbook of mathematical func-*  
712 *tions with formulas, graphs and mathematical tables*. National Bureau  
713 of Standards, 1964.
- 714 [47] I. Ginzburg and K. Steiner. A free-surface lattice Boltzmann method  
715 for modelling the filling of expanding cavities by Bingham fluids. *Phil.*  
716 *Trans. R. Soc. Lond. A*, 360:453–466, 2002.
- 717 [48] X. Yin, D.L. Koch, and R. Verberg. Lattice-Boltzmann method for sim-  
718 ulating spherical bubbles with no tangential stress boundary conditions.  
719 *Phys. Rev. E*, 73:1–13, 2006.

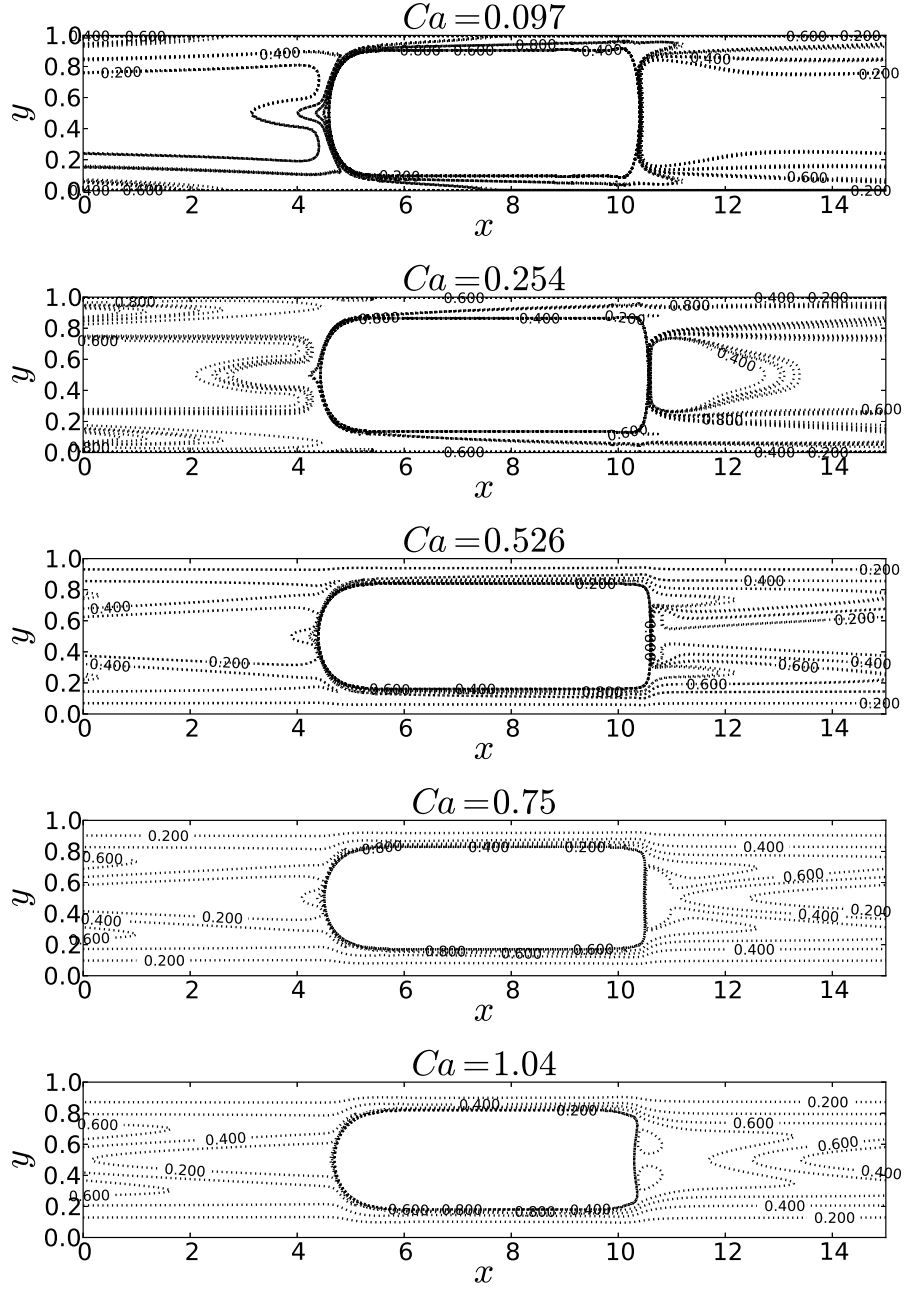


Figure 8: Concentration contour profiles for velocity scalings as identified in Table 2 (top to bottom:  $Ca = 0.097, 0.254, 0.526, 0.750, 1.040$ ). Lines correspond to all different scales indicated in Table 2 (top to bottom: 6 scalings, 5 scalings, 2 scalings, 1 scaling, 1 scaling). Some lines are indistinguishable showing that simulations with velocity scalings are consistent.

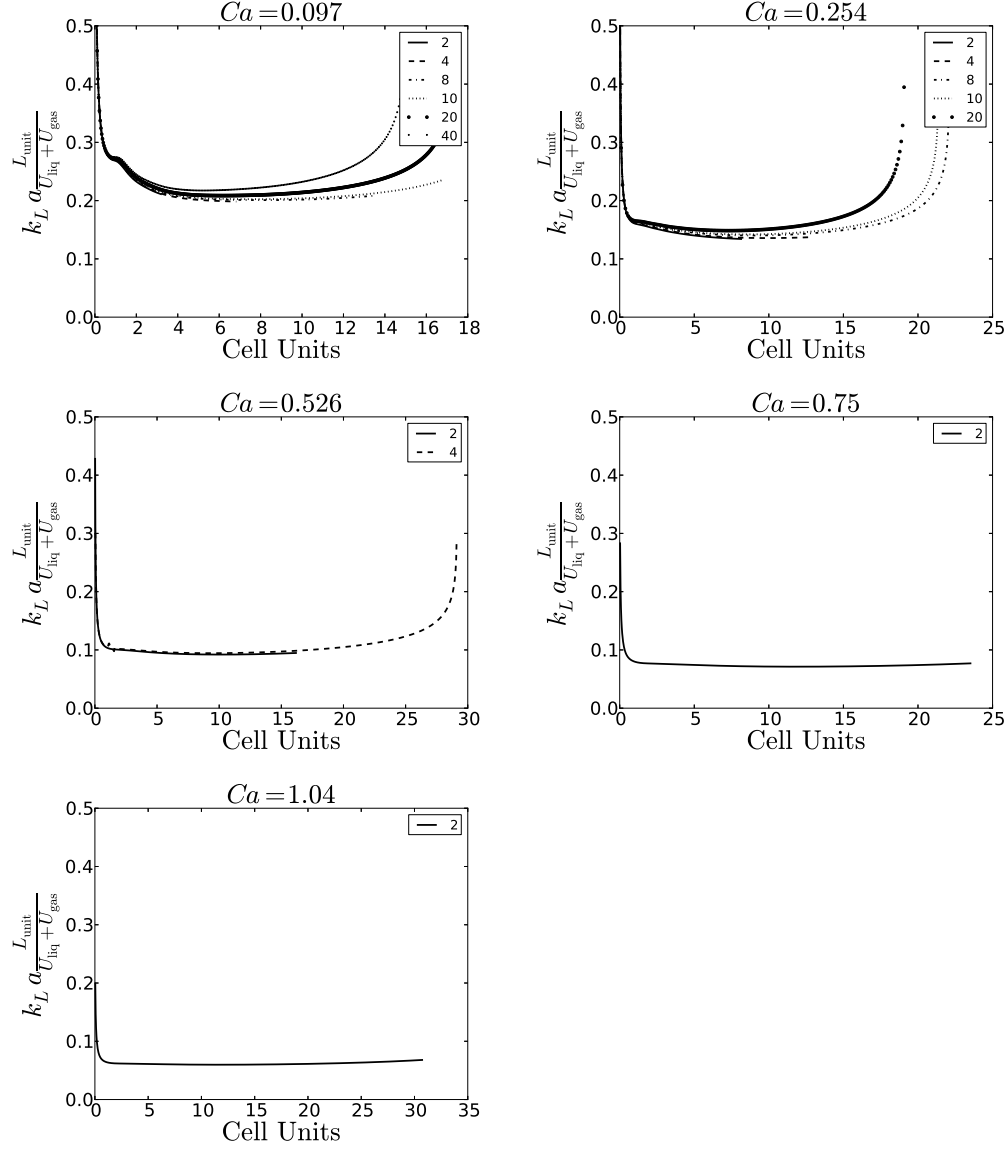


Figure 9: Volumetric mass transfer coefficient for different capillary numbers and scales against the bubble travel distance in the laboratory frame. "Cell Units" axis refers to the physical distance of how many unit cells the bubble travels until the steady state is reached. A legend is provided for velocity scalings. All of them show a good agreement. One can see an abnormal rise of the mass transfer coefficient when the average concentration is close to  $C^*$  due to the logarithmic function evaluation. Table 3 summarizes results presented here.

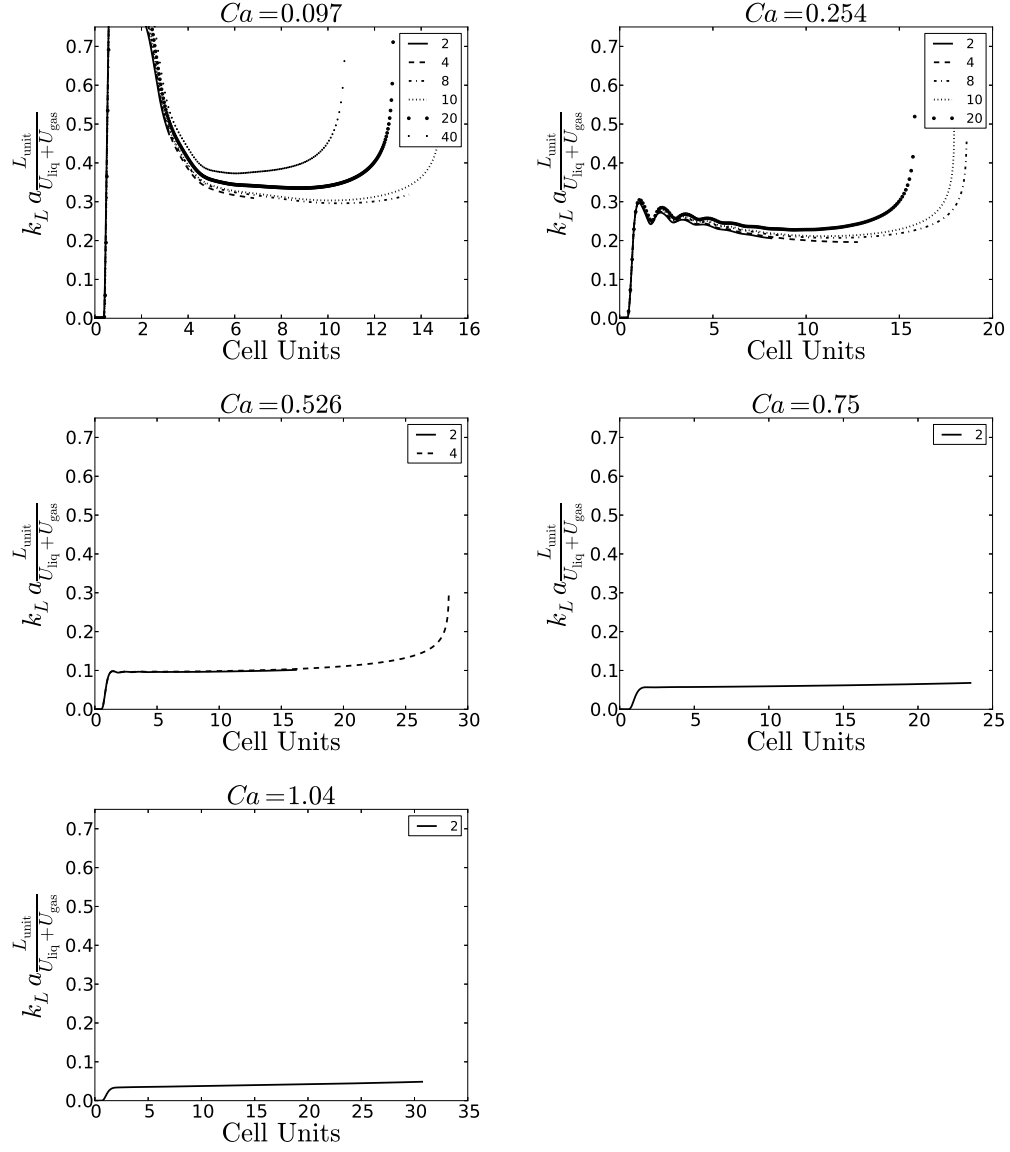


Figure 10: The volumetric mass transfer coefficient with the characteristic concentration based on the inlet/outlet flux averaged concentration as in [2]. One can see that depending on the velocity pattern, the values are either overpredicted or underpredicted in comparison to values specified in Table 3



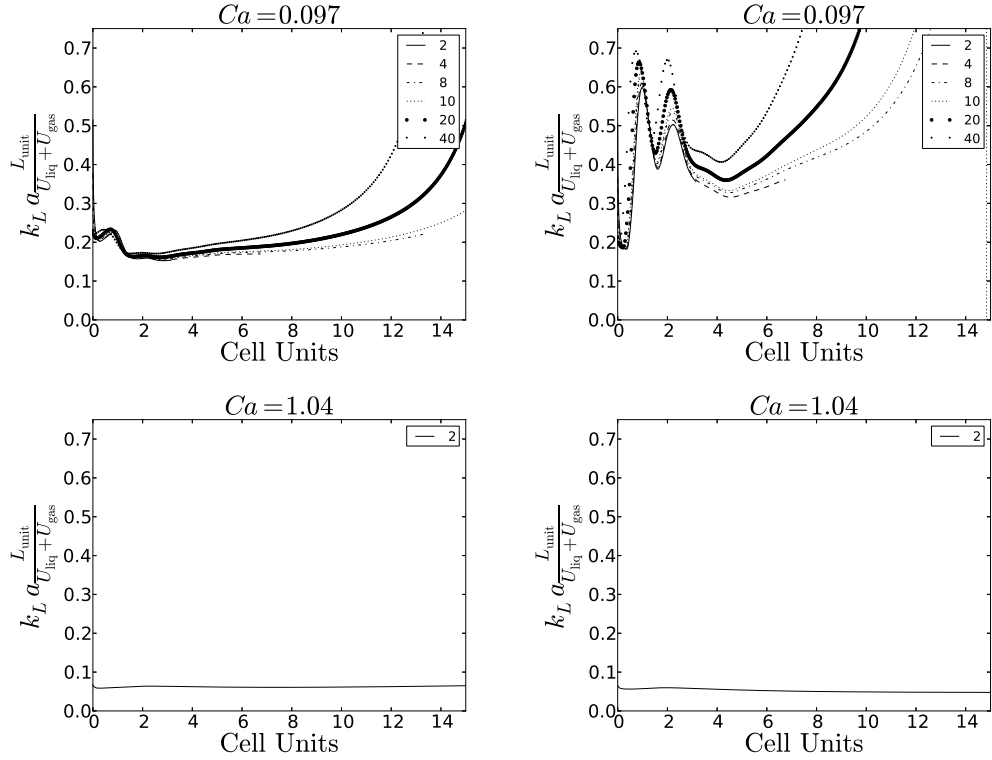


Figure 11: The van Baten and Krishna [2] formulations for  $Ca = 0.097$  (top) and  $Ca = 1.04$  (bottom) with the characteristic concentration being domain-averaged (left) and inlet/outlet flux-averaged (right). One can see that the van Baten and Krishna [2] formulation produces good results with the characteristic concentration being the average concentration. Moreover, the values are closer to values obtained with many cell simulations, see Fig. 12, than in comparison with periodic boundary simulations in Section 5.2. However, the characteristic concentration being inlet/outlet flux-averaged does not produce consistent results.

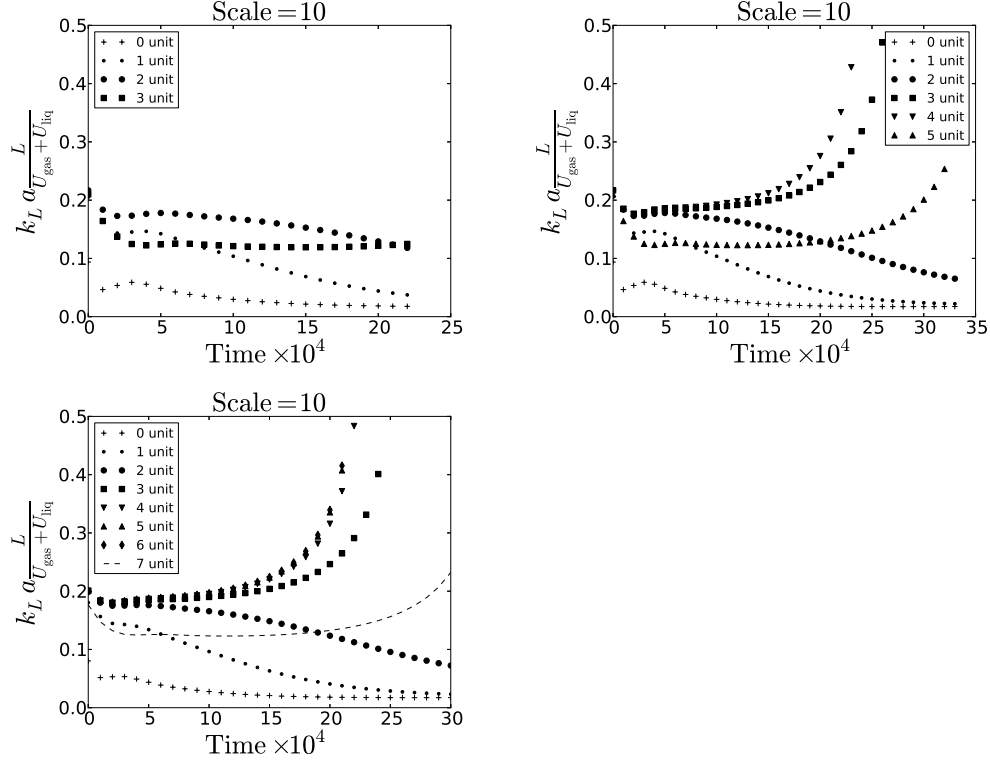


Figure 12: The non-dimensional volumetric mass transfer coefficient defined in Eq. 34 for 4 (top left), 6 (top right), 8 unit cells (bottom). Only scale 10 is presented since all other simulations produce the same results. One can see that 4 unit cells is not enough to avoid the influence of boundaries. However, the results for 6 and 8 unit cells are consistent and show that beginning from third unit cell the results and ending with the penultimate cell results are consistent with periodic boundary simulations and van Baten and Krishna [2] formulations.

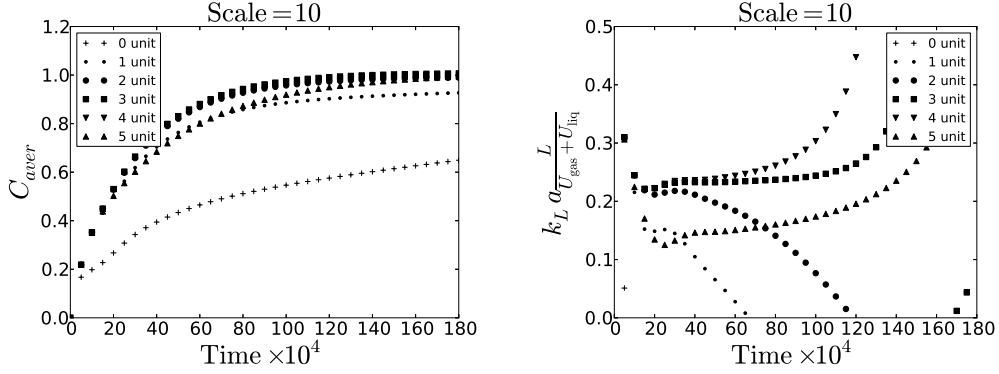


Figure 13: Average concentrations (left) and volumetric coefficients (right) for 6 unit cells. The volumetric mass transfer coefficient is calculated based on Eq. 35 and accounts for inlet and outlet fluxes.

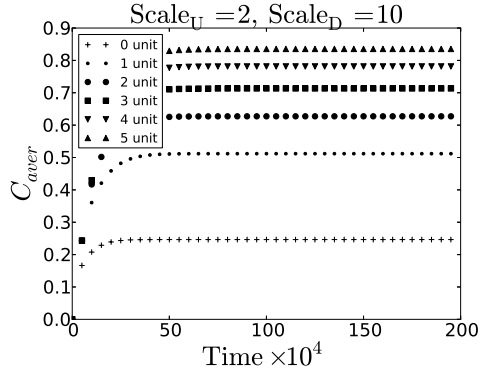


Figure 14: Results for 6 unit cells. The Peclet number equals to  $Pe = 2644$ . One can see that average concentrations reach certain value and stay constant. Thus, the volumetric mass transfer coefficient,  $k_L a \frac{L_{unit}}{U_{bubble} + U_{gas}}$ , can be calculated using the spatial approach, see Fig. 15.

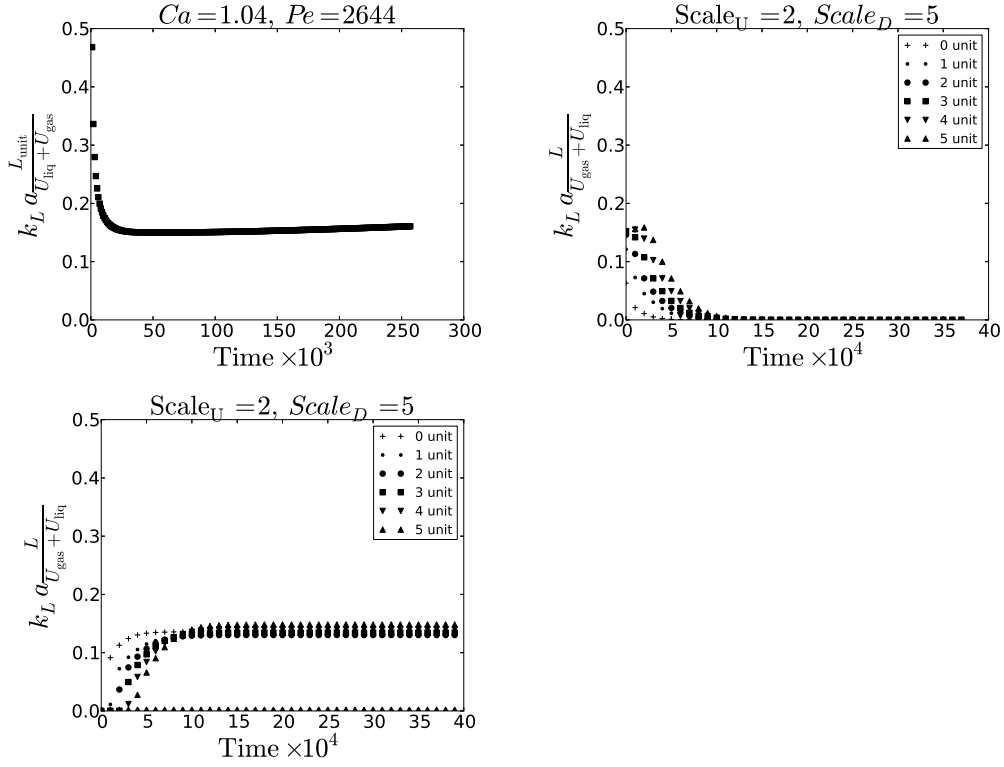


Figure 15: The periodic (top left, 1 unit cell, Eq. 13), unit cells domain-averaged concentrations as a function of time (top right, 6 unit cells, Eq. 13), and spatial location (bottom, 6 unit cells, Eq. 36) calculated volumetric mass transfer coefficients. One can see that they all coincide. However, the calculations based on periodic boundary conditions produce a slightly overestimated volumetric mass transfer coefficient. One can as well see that the domain-averaged concentration simulations (top right) reach the steady volumetric concentration fast and start decaying after that. It is not convenient to use them in practical cases for unmixed slug, i.e.  $Ca > 0.7$ .

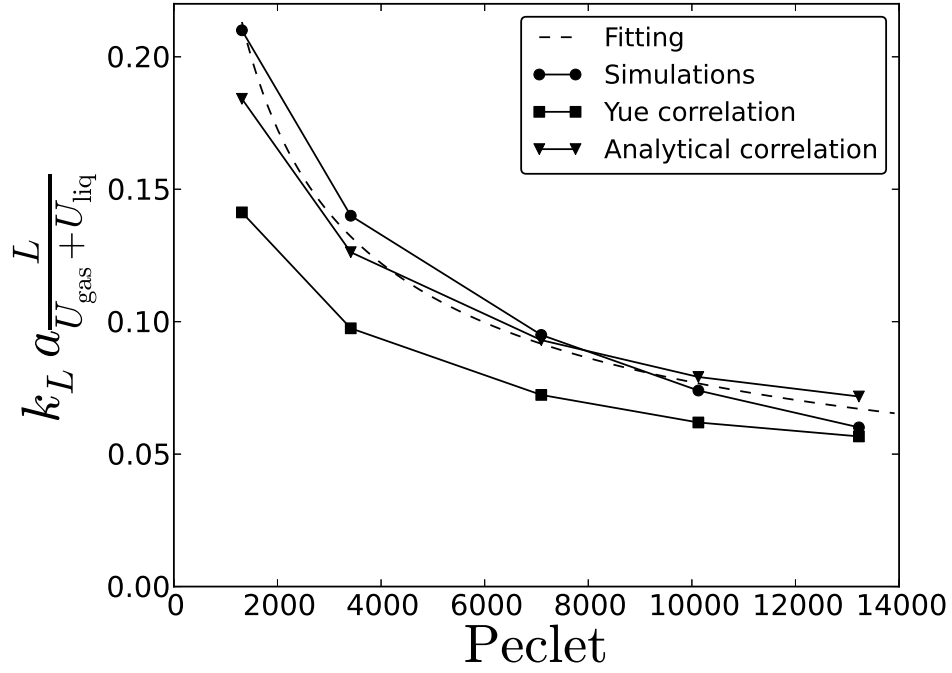


Figure 16: Comparison between the correlation by Yue et al. [7], the analytical correlation derived by following the work [15] and the mass transfer coefficient based on periodic boundary conditions. The fitting curve ( $7.745Pe^{-0.50038}$ ) is proportional to  $Pe^{-0.5}$  which corresponds to all correlations. One can as well see that the deviation from the analytical expression becomes larger with the increasing Peclet number, which happens because the analytical expression does not account for the velocity pattern and the bubble shape change.

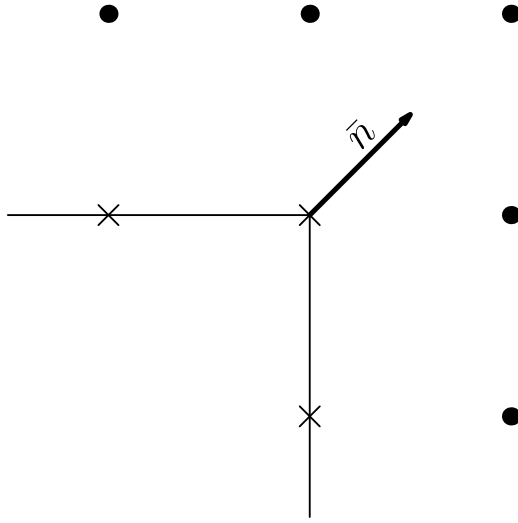


Figure 17: Free-surface boundary condition represented in the lattice Boltzmann method. Boundary nodes are depicted by crosses, and fluid nodes are represented by dots. The populations at the corner boundary nodes are essentially the populations of the fluid node, but in a different order.